Dalton Transactions

ROYAL SOCIETY OF CHEMISTRY

PAPER

View Article Online
View Journal | View Issue

Cite this: *Dalton Trans.*, 2023, **52**, 10386

Deciphering the role of water and a zinc-doping process in a polyol-based approach for obtaining Zn/Co/Al-based spinels: toward "green" mesoporous inorganic pigments†

Maria-Gabriela Alexandru, [a] Adelina-Carmen Ianculescu,*[b] Oana Carp,[c] Daniela C. Culita, [c] Silviu Preda, [c] Cristian D. Ene, [c] Bogdan Stefan Vasile, [b] Vasile-Adrian Surdu, [b] Adrian-Ionut Nicoara,[b] Florentina Neatu, [d] Ioana Pintilie [d] and Diana Visinescu *[c]

Two new families of zinc/cobalt/aluminum-based pigments, with a unique composition, were obtained through the polyol method. The hydrolysis process of a mixture of $Co(CH_3COO)_2$, $Zn(acac)_2$ and $Al(acac)_3$ ($acac^-$ = acetylacetonate ion) in 1,4-butanediol afforded dark blue gels (***w*PZn$_x$Co$_{1-x}$Al**), in the presence of a supplementary amount of water, and light green powders (***P*Zn$_x$Co$_{1-x}$Al**), respectively, for the water-free procedure (x = 0, 0.2, 0.4). The calcination of the precursors yielded dark green (***w*Zn$_x$Co$_{1-x}$Al**) and blue (**Zn$_x$Co$_{1-x}$Al**) products. XRD measurements and Rietveld refinement indicate the co-existence of three spinel phases, in different proportions: $Zn_xCo_{1-x}Al_2O_4$, Co_3O_4 and the defect spinel, γ-$Al_{2.67}O_4$. The Raman scattering and XPS spectra are in agreement with the compositions of the samples. The morphology of ***w*Zn$_x$Co$_{1-x}$Al** consists of large and irregular spherical particle aggregates (*ca*. 5–100 mm). Smaller agglomerates (*ca*. 1–5 mm) with a unique silkworm cocoon-like hierarchical morphology composed of cobalt aluminate cores covered with flake-like alumina shells are formed for **Zn$_x$Co$_{1-x}$Al**. TEM and HR-TEM analyses revealed the formation of crystalline, polyhedral particles of 7–43 nm sizes for ***w*Zn$_x$Co$_{1-x}$Al**, while for **Zn$_x$Co$_{1-x}$Al**, a duplex-type morphology, with small (7–13 nm) and larger (30–40 nm) particles, was found. BET assessment showed that both series of oxides are mesoporous materials, with different pore structures, with the water-free samples exhibiting the largest surface areas due, most likely, to the high percent of aluminum oxide. A chemical mechanism is proposed to highlight the role of the water amount and the nature of the starting compounds in the hydrolysis reaction products and, further, in the morpho-structural features and composition of the resulting spinel oxides. The CIE $L^*a^*b^*$ and C^* colorimetric parameters indicate that the pigments are bright, with a moderate degree of luminosity, presenting an outstanding high blueness.

Received 29th March 2023,
Accepted 20th June 2023

DOI: 10.1039/d3dt00972f

rsc.li/dalton

[a]*Department of Inorganic Chemistry, Physical Chemistry and Electrochemistry, Faculty of Chemical Engineering and Biotechnologies, University Politehnica of Bucharest, 1-7 Gh. Polizu Street, 011061 Bucharest, Romania*
[b]*Department of Science and Engineering of Oxide Materials and Nanomaterials, University Politehnica of Bucharest, Bucharest, 060042, Romania. E-mail: adelina.ianculescu@upb.ro*
[c]*"Ilie Murgulescu" Institute of Physical Chemistry, Romanian Academy, 202 Splaiul Independentei, 060021 Bucharest, Romania. E-mail: diana.visinescu@gmail.com*
[d]*National Institute of Materials Physics, P.O. Box MG-7, Bucharest-Magurele 077125, Romania*

† Electronic supplementary information (ESI) available: FTIR spectra (Fig. S1 and S2) and NIR-UV-Vis spectra (Fig. S3 and S4) of ***w*PZn$_x$Co$_{1-x}$Al** and ***P*Zn$_x$Co$_{1-x}$Al**. XRD patterns (Fig. S5), PL spectra (Fig. S6), SEM micrographs (Fig. S7 and S8) and EDX analysis results (Fig. S9) of ***P*Zn$_x$Co$_{1-x}$Al**. TG, DTG and DSC curves of ***w*PZn$_x$Co$_{1-x}$Al** (Fig. S10 and S11) and ***P*Zn$_x$Co$_{1-x}$Al** (Fig. S12 and S13) precursors (x = 0.2, 0.4). Results of the Rietveld refinement on the XRD data for ***w*Zn$_x$Co$_{1-x}$Al** (Fig. S14–S16) and **Zn$_x$Co$_{1-x}$Al** (Fig. S17–S19) oxides. Raman spectra for **Zn$_x$Co$_{1-x}$Al** oxides (Fig. S20). High-resolution C 1s XPS spectra for ***w*ZnxCo$_{1-x}$Al** and **ZnxCo$_{1-x}$Al** oxides (Fig. S21). N_2 adsorption–desorption isotherms of ***w*Zn$_x$Co$_{1-x}$Al** (Fig. S22–S24) and **Zn$_x$Co$_{1-x}$Al** (Fig. S25–S27) oxides. Overlaid FTIR spectra (Fig. S28–S30) and NIR-UV-Vis spectra (Fig. S31 and S32) of ***w*Zn$_x$Co$_{1-x}$Al** and **Zn$_x$Co$_{1-x}$Al** oxides, schematic representation of the two-step polyol-assisted reaction including pictures of the water-added, ***w*PZn$_x$Co$_{1-x}$Al**, and water free, ***P*Zn$_x$Co$_{1-x}$Al**, precursors and their thermolysis products, ***w*Zn$_x$Co$_{1-x}$Al** and **Zn$_x$Co$_{1-x}$Al** oxides (Fig. S33). Results of the XPS survey scan (Table S1) and EDX energies (eV) and atomic ratio (%) of water-added ***w*Zn$_x$Co$_{1-x}$Al** and water-free **Zn$_x$Co$_{1-x}$Al** oxides (Table S2). See DOI: https://doi.org/10.1039/d3dt00972f

Introduction

Metal aluminates, $M^{II}Al_2^{III}O_4$, with a cubic spinel structure, represent a fascinating family of multifunctional ternary oxides, with different applications as (photo)catalysts,[1–6] adsorbents,[7] magnetic materials,[8] humidity and gas sensors[9,10] and, more recently, for energy storage.[11] In particular, cobalt aluminate ($CoAl_2O_4$), known as Thénard's Blue (TB) or cobalt blue pigment, is an old and famous high-quality blue pigment, with significant photo-/thermochemical stability, superior coloring properties and an extraordinary resistance to corrosion. Nowadays, $CoAl_2O_4$ is largely used for the coloration of ceramic bodies, plastics, paint, paper, concrete, and fibers, or as a contrast-enhancing luminescent pigment with self-cleaning abilities.[12–15] The typical and intense blue color of TB is mainly due to the strong preference of Co^{2+} ions for the tetrahedral sites within the cubic lattice of the normal spinel-type $A^{II}B_2^{III}O_4$, whereas its green color is characteristic of an inverse spinel structure, with the Co^{2+} ions located in octahedral sites.[16–18] The color and coloring capabilities of the cobalt aluminates strongly depend on their phase purity, as well as on their morphological (sizes, shapes and textures) and structural (crystallinity degree and inversion degree) characteristics.[19,20]

The ceramic synthesis of the $CoAl_2O_4$ pigment, based on a solid-state reaction between individual oxides (CoO or Co_3O_4 and α-Al_2O_3, respectively), represents the conventional route in the synthesis of metal aluminate oxides. Such a procedure demands high temperature (*ca.* 1300 °C), long reaction time and extended grinding process to obtain low-sized pigments with superior hiding properties.[21,22] For obtaining high-performance materials a certain degree of control on their morpho-structural features and composition is required. Therefore, the development of soft chemistry approaches for the synthesis of nanomaterials accelerated the transition toward the next generation of inorganic multifunctional oxide-based pigments.[23] From the numerous advantages provided by the soft chemistry synthesis, it is worth mentioning the economical aspects (low energy consumption, shorter reaction times, and cheap raw materials) and, also, the large perspectives opened in the design of mixed oxides, containing different metal ions, with various stable oxidation states and preferred geometries that particularly influence the color of the pigments.[24–28] Intense efforts have been made to develop efficient synthetic methods of cobalt aluminate that, on one hand, could provide the best pigment characteristics, and, on the other hand, reduce the toxic effect of Co^{2+} ions from $CoAl_2O_4$ on the human health and environment, by partially replacing Co^{2+} with non-toxic metal ions.[29,30] Thus, sol–gel,[8,15] hydrothermal,[31,32] reverse microemulsion,[26] low-temperature thermolysis of heteronuclear coordination compounds,[33] combustion,[34–36] and co-precipitation methods[37] were commonly employed in the synthesis of nano-sized aluminates with improved optical and coating properties. Besides, such synthesis routes opened interesting "green" alternatives by replacing harmful raw materials with eco-friendly ingredients (as polysaccharides).[2,38] In the case of TB, the gradual substitution of the toxic cobalt(II) ions with the non-hazardous metal cations (like Zn^{2+}, Ca^{2+} or Mg^{2+}), by preserving and even improving their chromaticity, represents a step forward toward eco-friendly inorganic pigments.[2,38–43]

The (poly)alcohol synthesis is one of the most convenient, resourceful, and straightforward soft chemistry routes to obtain well-crystallized metals or metal oxides with high compositional homogeneity, diversity of shapes, assembly motifs, and narrow size distributions.[44–46] Synthesis parameters like reaction time and/or temperature, the presence/absence of reaction additives, as well as the concentration of the metal precursor, strongly influence the crystallite nucleation and growth kinetics, as well as the surface chemistry of the resulting oxide particles.[44–46] Moreover, many of the polyols are green solvents because they show low to moderate toxicity and are highly biodegradable. Polyol synthesis performed in various (ether)-diols, with different chain lengths, linear or branched, proved to be efficient for obtaining ternary oxides, with well-defined stoichiometry, such as spinel-type oxides, $M^{II}M_2^{III}O_4$ (M^{II} = Mg, Zn, Co, Ni, Mn; M^{III} = Fe, Co, Al).[47–49] Focusing on TB materials, the nature and concentration of the precursors, as well as the reaction temperature, have a significant effect on the structural and morphological characteristics of the oxides.[50,51]

Herein, we describe the synthesis and characterization (structural, morphological, and optical) of two new series of Zn/Co/Al oxide-based pigments, obtained through a hydrolysis process, in 1,4-butanediol, followed by the thermolysis of the as-obtained precursors. The morpho-structural investigation outlined the influence of the preparation method (the water amount, *in situ* generated or intentionally added, and the Zn^{II} cation incorporation process) on the composition of the precursors and, consequently, on the composition, size/shape, and texture of the corresponding oxide particles and, further, on their opto-chromatic properties.

Experimental

Materials and synthesis

Cobalt acetate [$Co(CH_3COO)_2{\cdot}4H_2O$, Sigma-Aldrich], zinc acetylacetonate [$Zn(C_5H_7O_2)_2{\cdot}H_2O$, Merck], aluminum acetylacetonate [$Al(C_5H_7O_2)_3$, Sigma-Aldrich] and 1,4-butanediol [$HO(CH_2)_4OH$, 1,4-BD, >99.5%] of analytical grade were used without further purification.

Sample notations. ***w*PZn$_x$Co$_{1-x}$Al** and ***P*Zn$_x$Co$_{1-x}$Al** (x = 0, 0.2 and 0.4) represent the precursors obtained in water-assisted and water-free synthesis, respectively, while ***w*Zn$_x$Co$_{1-x}$Al** and **Zn$_x$Co$_{1-x}$Al** are the corresponding oxides obtained after calcinations of the precursors for 1 h at 800 °C. We denominate the reaction products obtained through the polyol-assisted synthesis, without any water addition, as "water-free", although a small amount of water is generated during the reaction.

Synthesis. The water-assisted ***w*PZn$_x$Co$_{1-x}$Al** precursors were obtained following a general procedure: zinc acetylacetonate (0 mmol, 0 g; 2 mmol, 0.53 g; 4 mmol, 1.05 g, respectively),

cobalt acetate (10 mmol, 2.49 g; 8 mmol, 1.99 g; 6 mmol, 0.74 g, respectively), and aluminum acetylacetonate (20 mmol, 6.48 g), were dissolved in 1,4-butanediol (25 ml), mixed and heated (up to 140 °C) under stirring in a round-bottom flask fitted with a reflux column. After 1 h, in the dark blue solution formed, 1 ml of water is added at the same time as the temperature rises to 180 °C, at which it is maintained for 12 h to afford dark-blue gels. The water-free light green powders of ***P*Zn$_x$Co$_{1-x}$Al** type precursors were obtained in a similar manner, except that no supplementary water was added in the reaction. After cooling at room temperature, both series of precursors were collected by centrifugation and washed with ethanol. The ***w P*Zn$_x$Co$_{1-x}$Al** gels were dried in an oven at 80 °C for 12 h. The thermal processing of the precursors at 800 °C for 1 h led to dark green (***w*Zn$_x$Co$_{1-x}$Al**) and intense blue (**Zn$_x$Co$_{1-x}$Al**) powders, respectively.

Thermal investigations

The thermal analysis has been carried out in alumina crucibles under static air, with a sample mass of *ca*. 10 mg at a heating rate of 5 K min^{-1} on a NetzchSTA 409 PC/PG thermobalance.

Spectral investigations

The IR spectra (KBr pellets) were recorded in the 4000–400 cm^{-1} range, with a FTIR Brucker Tensor V-37 spectrophotometer. NIR-UV-Vis spectra (diffuse reflectance technique) were recorded on a 200–1800 nm domain with a JASCO V-670 spectrophotometer, using MgO as the standard. The diffuse reflectance of the samples was measured with a PerkinElmer Lambda 35 spectrophotometer, in the 300–800 nm range, using standard D65 illumination. The CIE-$L^*a^*b^*$ colorimetric method, recommended by the Commission Internationale de l'Eclairage (CIE), was followed: L^* is the lightness axis [black (0) → white (100)], b^* is the blue (−) → yellow (+) axis, and a^* is the green (−) → red (+) axis. The parameter C^* (chroma) represents the saturation of the colour, being defined as:

$$C^* = \sqrt{(a^*)^2 + (b^*)^2}$$

Raman spectroscopy analyses were carried out at room temperature to investigate the local order in the spinel powders. The spectra were recorded using a LabRaman HR Evolution spectrometer (Horiba, Kyoto, Japan) with a 514 nm line of an argon ion laser, by focusing a 125 mW beam of a few micrometer sized spots on the samples under investigation. An acquisition time of 10 s was established for each of the 80 accumulations during the investigation.

Structural and morphological investigations

X-ray diffraction-XRD analysis. Powder X-ray diffraction (XRD) patterns were collected at room temperature using the theta–theta geometry on a PANalytical Empyrean X-ray diffractometer, with CuKα radiation (λ = 1.5406 Å) operating at 45 kV and 40 mA. Counts were collected in the 2θ range of 10°–80°, with a step size of 0.02° and time per step of 255 seconds with a PIXCel3D detector operated in line scanning mode. The pulse height discrimination levels were set to a minimum of 40% and a maximum of 80% in order to remove the fluorescence signal from cobalt ions in the powders. PXRD data were analyzed using HighScorePlus 3.0e software, with a whole pattern profile fitting (WPPF) module, connected to ICDD PDF4 + database. Crystallite size *D*, micro-strains and unit cell parameters were estimated from PXRD data using the Rietveld refinement method.

X-ray photoelectron spectroscopy – XPS measurements. The equipment used for XPS analysis was an AXIS Ultra DLD (Kratos Analytical Ltd, Manchester, UK). For the measurements the following parameters were used: monochromated Al Kα ($h\nu$ = 1486.7 eV) radiation of an X-ray gun power of 144 W (12 kV/12 mA), and a pressure of 1×10^{-8} Pa. A charge neutralizer was used (electron acceleration at 1 eV and an electron current of 0.1 mA) to avoid charge effects for all samples. All the samples were calibrated at the C 1s line (BE = 284.6 eV, C–C $(CH)_n$ bonds) of the adsorbed hydrocarbon on the sample surface. The experimental results were analyzed in Igor Pro8 from Wavemetrics, using the XPST plug-in.

Scanning electron microscopy – SEM and (high resolution)-transmission electron microscopy – (HR)-TEM analyses. To analyze the oxide particle size, morphology, and crystallinity degree and to check the chemical composition, purity and chemical homogeneity, SEM, TEM and HRTEM coupled with SAED (surface area electron diffraction) and EDX (energy dispersive X-ray spectroscopy) investigations were performed using a high-resolution FEI QUANTA INSPECT F Scanning Electron Microscope (SEM) with a field emission gun and a TITAN THEMIS Ultra high Resolution Electron Microscope (TEM/HRTEM) from Thermo Fisher Scientific. For the acquisition of the EDX spectra and elemental maps, the transmission electron microscope was operated in STEM (scanning transmission electron microscopy) mode at 300 kV using a HAADF (high-angle annular dark-field) detector for imaging and an in-column windowless 4 Super EDX detector for elemental analysis.

Gas porosimetry analysis. The porosity and surface area of the powdered samples were determined by nitrogen adsorption–desorption analysis at −196 °C using a Micrometrics ASAP 2020 analyzer. Specific surface areas (S_{BET}) were calculated according to the Brunauer–Emmett–Teller (BET) equation. The total pore volume (V_{total}) was estimated from the amount adsorbed at a relative pressure equal to 0.99. The pore size distribution curves were obtained from the adsorption branch using a DFT model.

Results and discussion

Synthesis and characterization of *w P*Zn$_x$Co$_{1-x}$Al and *P*Zn$_x$Co$_{1-x}$Al precursors (x = 0, 0.2, 0.4)

The reaction of zinc(II) acetylacetonate, cobalt(II) acetate and aluminum(III) acetylacetonate with an [xZn^{2+} + (1 − x)

Co^{2+}]:$2Al^{3+}$ stoichiometry in 1,4-butanediol afforded two types of products, depending on the water amount in the reaction: dark blue gels (***w*PZn$_x$Co$_{1-x}$Al**) in water-assisted synthesis and light green powders (***P*Zn$_x$Co$_{1-x}$Al**) in reactions carried out without the addition of an extra amount of water (x = 0, 0.2, 0.4). Generally, metal substituted cobalt aluminates were obtained by a gradual incorporation of cobalt(II) ions into a non-hazardous $M^{II}Al_2^{III}O_4$ host lattice (M = Zn, Mg).[25,38,40–42] Herein, we investigated a reversed incorporation procedure, in which the cobalt(II) ions are progressively replaced by zinc(II) cations within the $CoAl_2O_4$ host spinel matrix.

A preliminary characterization of the water-added/free precursors has been carried out through FTIR and NIR-UV-Vis spectroscopy as well as through thermal analysis. FTIR measurements were performed on the ***w*PZn$_x$Co$_{1-x}$Al** and ***P*Zn$_x$Co$_{1-x}$Al** precursors to reveal the nature of the formed compounds by detecting the functional groups through the specific vibrations of C–H/C–OH/C═O/O–H bonds (3500–1000 cm^{-1} range) and, also of the M–O bonds (covering the 900–400 cm^{-1} region). Thus, the FTIR spectra of the ***w*PZn$_x$Co$_{1-x}$Al** and ***P*Zn$_x$Co$_{1-x}$Al** precursors show the formation of two different types of compounds (Fig. S1 and S2 and detailed discussion in the ESI†), suggesting the formation of different intermediates, with bands at 1400–1720 and 1000–1100 cm^{-1} specific for hydroxide and/or hydroxyacetate, diol/acac complexes,[52,53] as well as between 400 and 900 cm^{-1}, characteristic of M–O bonds.[54] For the ***P*Zn$_x$Co$_{1-x}$Al** precursor, typical absorptions of boehmite, γ-AlO(OH), occurred: two intense bands at 1107 and 1036 cm^{-1} stand for symmetric (δ_s) and asymmetric (δ_{as}) bending vibrations of Al–O–H, while torsional, stretching and bending modes of Al–O bonds occur at 776, 636 and 485 cm^{-1} as medium/weak intensity bands.[55] Also, NIR-UV-Vis spectroscopy measurements were carried out on the two types of precursors to probe the electronic transition of the metal ions, especially for the tetrahedral Co(II) cations that exhibit typical d–d electronic transitions in visible and near-infrared regions. The NIR-UV-Vis spectra for both water-assisted, ***w*PZn$_x$Co$_{1-x}$Al**, and water-free, ***P*Zn$_x$Co$_{1-x}$Al**, precursors show absorption bands attributed to d–d transitions of tetrahedral cobalt(II) ions (Fig. S3 and S4 of ESI†).[38] The PXRD patterns confirm the resemblances of the water-free precursors, independent of the Co^{2+}/Zn^{2+} ratio (Fig. S5 of ESI†), the peaks at (020), (120), (031) and (200) being attributed to the orthorhombic γ-AlO(OH) and/or incipient spinel phases. Besides, boehmite exhibits blue emission under visible excitation wavelength, due to oxygen vacancies and hydroxyl groups bound to surface aluminum (AlOH) centers.[56] The photoluminescence spectra of the ***P*Zn$_x$Co$_{1-x}$Al** precursors also exhibit typical boehmite broad emission centered at *ca.* 460 nm (λ_{exc} = 400 nm, Fig. S6 of ESI†),[56] whereas the EDX analysis of the richest zinc(II) precursor (x = 0.4) shows the predominance of the Al element in the cocoon-like aggregates (Fig. S7–S9 of ESI†).

Thermal analysis. To survey the thermolysis process and the decomposition of the water added, ***w*PZn$_x$Co$_{1-x}$Al**, and water free, ***P*Zn$_x$Co$_{1-x}$Al**, precursors, TG-DTG/DSC measurements were performed in the 25–1000 °C temperature range. The thermochemistry of the two series of precursors, ***w*PZn$_x$Co$_{1-x}$Al** and ***P*Zn$_x$Co$_{1-x}$Al**, is clearly influenced by the reaction conditions (Fig. 1 and Fig. S10–S13 of the ESI†): the thermal decomposition consists of two initial endothermic processes (except for ***P*Zn$_x$Co$_{1-x}$Al**, x = 0.4, for which three decomposition steps are identified), followed by a complex exothermic decomposition stage composed of a succession of overlapped thermal processes. For both series of precursors, the first step occurs up to *ca.* 140 °C and is assigned to the adsorbed water liberation. As expected, the dark blue gels, corresponding to the ***w*PZn$_x$Co$_{1-x}$Al** precursors, contain more water (adsorbed or coordinated) than the water-free analogues: for x = 0, the weight loss is *ca.* 11.2% for the water-added sample compared to *ca.* 3.8% for the water-free precursor. The second step takes place at relatively high temperatures (up to *ca.* 245 °C) and could be caused by the oxidative fragmentation of the organic residue, with the occurrence of a weak exothermic effect supporting this presumption (red arrow in Fig. 1a). The next weight loss stage (up to *ca.* 450 °C) represents the degradation/combustion process of the organic components, which, in the case of ***w*PZn$_x$Co$_{1-x}$Al** samples, occurs as a delimited step, although the related DSC curves exhibit two or three exothermic peaks (the strongest maximum being located at *ca.* 300 °C). For the ***P*Zn$_x$Co$_{1-x}$Al** precursors, the decomposition process takes place in two delimited steps, coupled with two exothermic peaks (maxima at *ca.* 300 and 390 °C).

The mass loss for water-free ***P*Zn$_x$Co$_{1-x}$Al** compounds is significantly higher than that for the water-assisted analogues

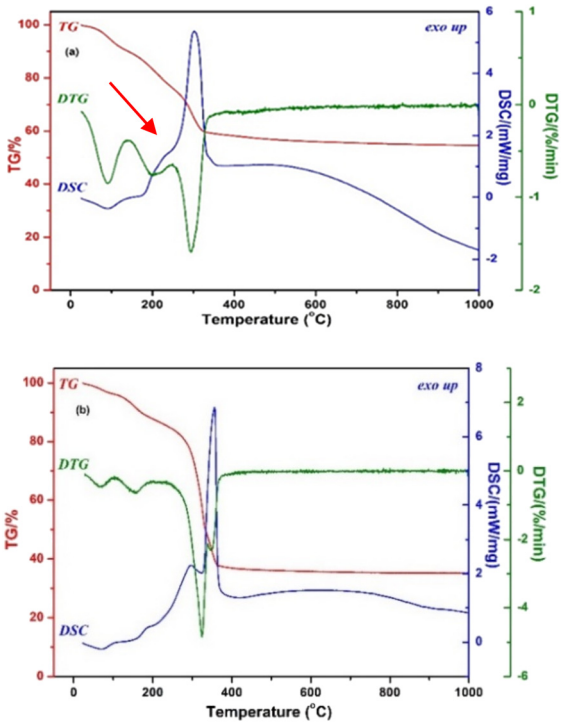

Fig. 1 Thermal curves (TG, DTG and DSC) for: water-assisted ***w*PZn$_x$Co$_{1-x}$Al** (top) and water-free ***P*Zn$_x$Co$_{1-x}$Al** (bottom) samples (x = 0).

(*e.g.* 51.3 *vs.* 18.3% for x = 0), due to a higher content of the organic residue. For both types of precursors, no resolved phase transformation is spotted at high temperatures. However, the broad and low intensity peak in the DSC curves, in the temperature range of 500–900 °C, could be attributed to the crystallization of the spinels. The thermal plots of the zinc-incorporated water-assisted samples have similar profiles to the zinc-free one, indicating a resembling thermal behavior (Fig. S10 and S12 of ESI†). Nevertheless, for x = 0.2, the second stage corresponding to the two overlapped processes of dehydration and degradation/combustion of organic materials is well-delimited, with a high weight loss (*ca.* 61%) occurring in the temperature range of 130–215 °C. This could be caused by a higher water content and/or hydroxy species that most likely are eliminated in this step. For ***P*Zn$_x$Co$_{1-x}$Al** precursors, the zinc doping process does not significantly affect the thermal behavior of the precursors, but the thermal effects are more delimited due to a higher compositional inhomogeneity induced by the zinc incorporation (Fig. S11 and S13 in the ESI†).

Characterization of the *w*Zn$_x$Co$_{1-x}$Al and Zn$_x$Co$_{1-x}$Al oxides (x = 0, 0.2, 0.4)

Structural investigation

X-ray diffraction. In the XRD patterns of the zinc/cobalt aluminate samples, ***w*Zn$_x$Co$_{1-x}$Al** and **Zn$_x$Co$_{1-x}$Al** oxides (x = 0, 0.2, 0.4), typical peaks of the spinel phase were identified (Fig. 2(a) and (b)). Nevertheless, a significant difference between the two groups of oxides was noticed.

Thus, well-delimited and sharp peaks, roughly assigned to the cobalt aluminate spinel (ICDD Card. No. 00-038-0814) for water-added samples, ***w*Zn$_x$Co$_{1-x}$Al**, *vs.* broadened peaks for water-free samples, were detected.[57–60] The larger peaks for the **Zn$_x$Co$_{1-x}$Al** samples could be the result of small sizes of the oxide particles and/or the presence of secondary crystalline phases, most likely also with a spinel structure. Indeed, the analysis of the XRD data indicates for the water-free oxides a high amount of alumina spinel ($Al_{2.67}O_4$), which becomes the major phase in the Zn-substituted samples (Table 1). From the results of the Rietveld refinement carried out on both ***w*Zn$_x$Co$_{1-x}$Al** and **Zn$_x$Co$_{1-x}$Al** oxides (Table 1 and Fig. S14–S19 in the ESI†), several conclusions should be outlined:

(i) For all samples, the best fit corresponds to a mixture of three spinel phases, *i.e.* iso-structural $CoAl_2O_4$, Co_3O_4 – guite (ICDD Card No. 00-043-1003), and the defect spinel, $Al_{2.67}O_4$ (ICDD Card No. 04-005-4662), except for **Zn$_x$Co$_{1-x}$Al** (x = 0.2) oxide in which only $CoAl_2O_4$ and $Al_{2.67}O_4$ crystalline phases were identified.

(ii) The highest proportion of crystalline $CoAl_2O_4$ was found for the water-assisted ***w*Zn$_x$Co$_{1-x}$Al** sample (x = 0.2), 83.3%, whereas, the water-free analogue, **Zn$_x$Co$_{1-x}$Al** (x = 0.2), contains the smallest amount of cobalt aluminate crystalline phase (3.9%). However, in the last case, the very low concentration of $CoAl_2O_4$ is most likely a result of the amorphous degree of the sample (crystallinity degree has the lowest value, 54.11%, Fig. 3 and Table 1).

(iii) The Zn-doping process has different effects on the oxide phase composition: for the water-assisted samples, ***w*Zn$_x$Co$_{1-x}$Al**, the gradual insertion of Zn(II) ions determines an increase of the Co_3O_4 concentration and a corresponding diminishment of $Al_{2.67}O_4$ content. Conversely, for the water-free **Zn$_x$Co$_{1-x}$Al** oxides, a reversed evolution of the alumina proportion occurred, increasing dramatically for x = 0.2 and x = 0.4, correlated with the low amount of Co_3O_4, down to 0 for x = 0.2 (Fig. 3).

(iv) The particle sizes are in the nanometer range and, for the water-assisted samples, they are generally higher than those of the water-free analogues.

(v) For the water-added oxides, ***w*Zn$_x$Co$_{1-x}$Al**, the Zn-doping process determines an increasing trend only for the aluminum oxide crystallites (from *ca.* 11 up to 25 nm), whereas Co_3O_4 has the highest crystallite size (*ca.* 57 nm). Conversely, for the water free **Zn$_x$Co$_{1-x}$Al** spinels, the Zn(II) cation incorporation process led to a decrease of the crystallite sizes of Zn/Co aluminates (from 26 down to 4.9 nm), whereas the aluminum oxide crystallite dimensions were not influenced by the doping process.

Raman spectra. Raman scattering provides additional information about the crystal structure and types of spinels in our samples. Thus, the Raman spectra, recorded on the water-assisted samples, ***w*Zn$_x$Co$_{1-x}$Al** (Fig. 4), revealed the presence of five main bands corresponding to the expected Raman active modes of a cubic spinel structure in the $Fd\bar{3}m$ spatial group: A_{1g} at 755 (vw) and 681/685 (s) cm^{-1}, $F_{2g}(3)$ at 613/

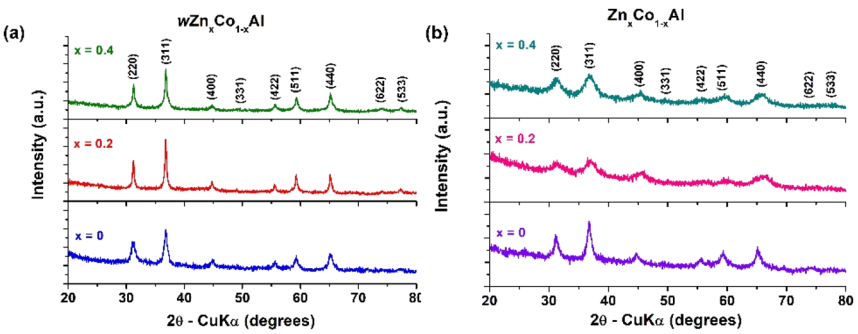

Fig. 2 PXRD patterns of the mixed oxides obtained after a heating treatment at 800 °C/1 h: (a) ***w*Zn$_x$Co$_{1-x}$Al** and (b) **Zn$_x$Co$_{1-x}$Al**.

Table 1 Phase composition and structural parameters obtained by Rietveld refinement[a]

	***w*Zn$_x$Co$_{1-x}$Al**			**Zn$_x$Co$_{1-x}$Al**		
	x = 0	x = 0.2	x = 0.4	x = 0	x = 0.2	x = 0.4
Phase composition	$CoAl_2O_4$ (81.6%) Co_3O_4 (3.9%) $Al_{2.67}O_4$ (14.5%)	$CoAl_2O_4$ (83.3%) Co_3O_4 (16.0%) $Al_{2.67}O_4$ (0.7%)	$CoAl_2O_4$ (73.3%) Co_3O_4 (19.8%) $Al_{2.67}O_4$ (6.9%)	$CoAl_2O_4$ (48.6%) Co_3O_4 (4.6%) $Al_{2.67}O_4$ (46.8%)	$CoAl_2O_4$ (3.9%) Co_3O_4 (0%) $Al_{2.67}O_4$ (96.1%)	$CoAl_2O_4$ (38.9%) Co_3O_4 (3.4%) $Al_{2.67}O_4$ (57.7%)
Symmetry	Cubic, $Fd\bar{3}m$	Cubic, $Fd\bar{3}m$	Cubic, $Fd\bar{3}m$	Cubic, $Fd\bar{3}m$	Cubic, $Fd\bar{3}m$	Cubic, $Fd\bar{3}m$
Unit cell parameters ($a = b = c$) (Å)	8.0928 ± 0.0037 ($CoAl_2O_4$) 8.0845 ± 0.0054 (Co_3O_4) 8.0210 ± 0.0185 ($Al_{2.67}O_4$)	8.0949 ± 0.0010 ($CoAl_2O_4$) 8.0978 ± 0.0054 (Co_3O_4) 8.0760 ± 0.0011 ($Al_{2.67}O_4$)	8.0959 ± 0.0025 ($CoAl_2O_4$) 8.0885 ± 0.0019 (Co_3O_4) 8.0276 ± 0.0011 ($Al_{2.67}O_4$)	8.0835 ± 0.0049 ($CoAl_2O_4$) 8.0899 ± 0.0051 (Co_3O_4) 8.0553 ± 0.0135 ($Al_{2.67}O_4$)	8.1376 ± 0.0101 ($CoAl_2O_4$) — (Co_3O_4) 7.9807 ± 0.0064 ($Al_{2.67}O_4$)	8.0885 ± 0.0194 ($CoAl_2O_4$) 8.0211 ± 0.0612 (Co_3O_4) 7.9489 ± 0.0109 ($Al_{2.67}O_4$)
Unit cell volume (Å^3)	530.0298 ($CoAl_2O_4$) 528.492 (Co_3O_4) 516.0363 ($Al_{2.67}O_4$)	530.4326 ($CoAl_2O_4$) 530.9946 (Co_3O_4) 526.7281 ($Al_{2.67}O_4$)	530.6428 ($CoAl_2O_4$) 529.1827 (Co_3O_4) 517.289 ($Al_{2.67}O_4$)	528.2087 ($CoAl_2O_4$) 529.457 (Co_3O_4) 522.6867 ($Al_{2.67}O_4$)	538.87 ($CoAl_2O_4$) — (Co_3O_4) 508.2983 ($Al_{2.67}O_4$)	529.1732 ($CoAl_2O_4$) 516.0634 (Co_3O_4) 502.2574 ($Al_{2.67}O_4$)
R expected, R_{exp}	6.46054	6.65252	6.89274	6.43947	6.44366	7.08213
R profile, R_p	6.04426	6.12248	6.3433	5.27937	4.69992	5.18676
Weighted R profile, R_{wp}	7.63774	7.9653	8.38335	6.70315	5.98996	6.72176
Goodness of fit, χ^2	1.39793	1.43362	1.47928	1.08357	0.86441	0.90082
Crystallinity	69.12	87.19	76.15	57.22	54.11	66.46
Crystallite sizes, <*D*> nm	9.83 ± 1.06 ($CoAl_2O_4$) 56.96 ± 3.93 (Co_3O_4) 10.76 ± 1.15 ($Al_{2.67}O_4$)	10.91 ± 7.69 ($CoAl_2O_4$) 28.48 ± 3.63 (Co_3O_4) 17.42 ± 10.65 ($Al_{2.67}O_4$)	7.94 ± 1.62 ($CoAl_2O_4$) 48.05 ± 6.23 (Co_3O_4) 24.60 ± 18.32 ($Al_{2.67}O_4$)	26.44 ± 5.51 ($CoAl_2O_4$) 7.36 ± 0.31 (Co_3O_4) 3.73 ± 4.16 ($Al_{2.67}O_4$)	7.23 ± 2.38 ($CoAl_2O_4$) — (Co_3O_4) 3.22 ± 1.75 ($Al_{2.67}O_4$)	4.90 ± 1.21 ($CoAl_2O_4$) 5.17 ± 1.53 (Co_3O_4) 4.44 ± 0.43 ($Al_{2.67}O_4$)
Internal strains, <*S*> (%)	1.02 ± 0.58 ($CoAl_2O_4$) 0.17 ± 0.07 (Co_3O_4) 0.86 ± 0.29 ($Al_{2.67}O_4$)	0.59 ± 0.75 ($CoAl_2O_4$) 0.17 ± 0.22 (Co_3O_4) 0.78± 0.63 ($Al_{2.67}O_4$)	1.31 ± 0.88 ($CoAl_2O_4$) 0.21 ± 0.11 (Co_3O_4) 0.55± 0.56 ($Al_{2.67}O_4$)	0.39 ± 0.31 ($CoAl_2O_4$) 1.32 ± 0.57 (Co_3O_4) 3.18 ± 1.62 ($Al_{2.67}O_4$)	0.81 ± 0.88 ($CoAl_2O_4$) — (Co_3O_4) 4.43 ± 2.22 ($Al_{2.67}O_4$)	2.08 ± 1.30 ($CoAl_2O_4$) 2.14 ± 1.31 (Co_3O_4) 2.25 ± 1.24 ($Al_{2.67}O_4$)

[a] ICDD cards used for indexing: $CoAl_2O_4$ – ICDD Card No. 00-038-0814; Co_3O_4 – ICDD Card No. 00-043-1003; and $Al_{2.67}O_4$ – ICDD card no. 04-005-4662.

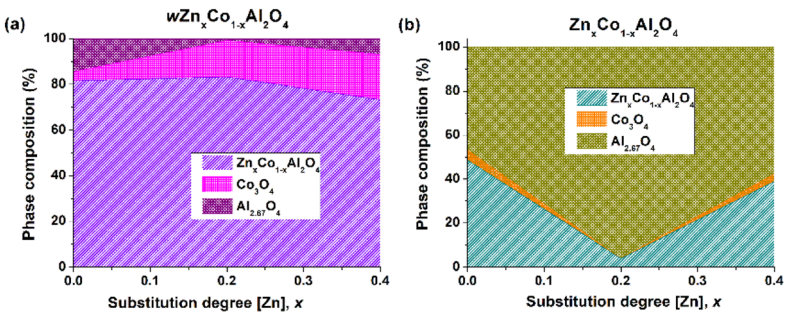

Fig. 3 Chart diagrams showing the variation of the phase composition depending on the zinc substitution degree (x) for: (a) water-assisted ***w*Zn$_x$Co$_{1-x}$Al** and (b) water-free **Zn$_x$Co$_{1-x}$Al** oxides.

619 cm^{-1}, $F_{2g}(2)$ at 516/520 cm^{-1}, E_g at 406 cm^{-1} and $F_{2g}(1)$ at *ca.* 191/194/197 cm^{-1}.[61,62]

The high energy phonon modes, A_{1g} and $F_{2g}(3)$, are generally correlated with M^{3+}–O stretching (symmetric and asymmetric) and bending vibrations from the octahedral MO_6 units of the spinel structure.[63,64] The occurrence of the two shoulders at 701 and 581 cm^{-1} in zinc-doped oxides could be related to the presence of a significant amount of Co^{3+} ions in the octahedral sites of the spinel lattice. The band located at 476 – 481 cm^{-1} and whose intensity increases for the zinc containing samples is generally attributed to the E_g vibration mode of Co_3O_4.[63,64] The lowest wavenumber band located between 191 and 197 cm^{-1} corresponds to the $F_{2g}(1)$ vibration and is attributed to the tetrahedral $Co^{II}O_4$ units.[64]

The zinc incorporation has multiple effects on the phonon vibrations due to the increase of the Co_3O_4 spinel content (see Table 1): a lower cobalt concentration determines a red shift of the translational motion of the entire tetrahedral AO_4 unit

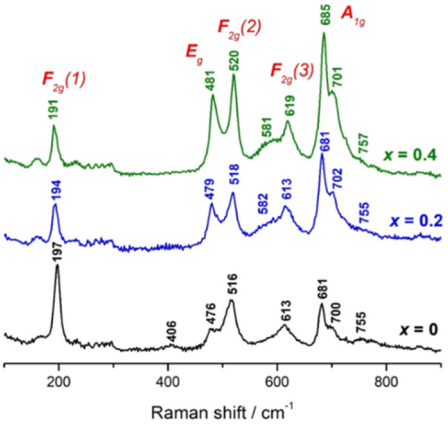

Fig. 4 Raman spectra for the water-assisted $w\mathbf{Zn_xCo_{1-x}Al}$ oxides (x = 0, 0.2, 0.4).

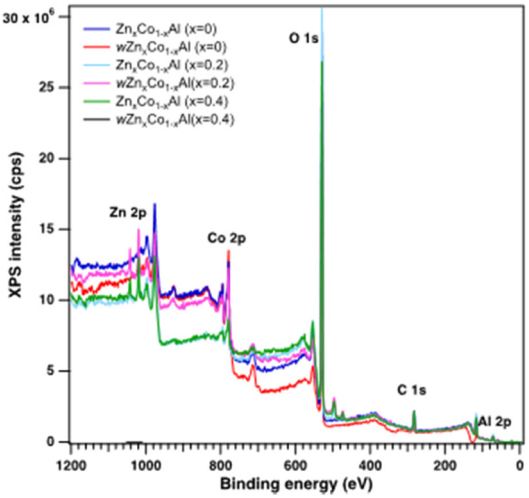

Fig. 5 Wide-scan X-ray photoelectron spectra of $w\mathbf{Zn_xCo_{1-x}Al}$ and $\mathbf{Zn_xCo_{1-x}Al}$ oxides (x = 0, 0.2, 0.4).

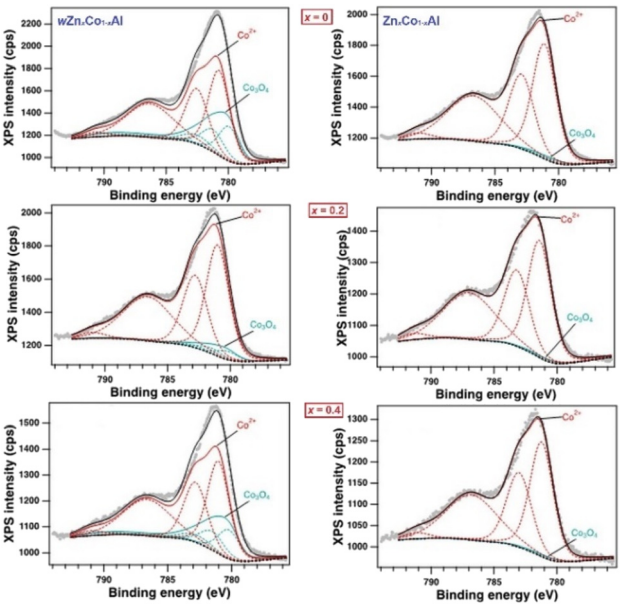

Fig. 6 High-resolution Co 2p XPS of the water-assisted $w\mathbf{Zn_xCo_{1-x}Al}$ and water-free $\mathbf{Zn_xCo_{1-x}Al}$ oxides (x = 0, 0.2 and 0.4).

within the lattice [$F_{2g}(1)$ mode] corroborated with the decrease of band intensity. Besides, for x = 0.2 and 0.4, a significant increase of the E_g mode band intensity, which depends on the octahedral sites, is also observed. The occurrence of a shoulder at *ca.* 580 cm^{-1} due to the vibration of Al–O bonds and $F_{2g}(3)$ symmetry indicates a change of the octahedral MO_6 units and this could also be correlated with a higher concentration of the octahedral Co^{3+} sites. However, many factors could interfere and deform/shift the Raman vibrations, like cation disorder, non-stoichiometry, or defects as well as the hierarchical arrangement of spinel nanoparticles.[64,65] The water-free $\mathbf{Zn_xCo_{1-x}Al}$ oxides show very weak Raman bands, and only for x = 0 all the vibrations corresponding to the spinel structure (190, 482, 518, 610, 682 and 740 cm^{-1} respectively; see Fig. S20 of the ESI†) are identified. The gradual incorporation of Zn^{2+} ions cancels the Raman phonon vibrations, most likely because of the Raman inactive $Al_{2.67}O_4$ formation.[66]

X-ray photoelectron spectroscopy (XPS). XPS measurements were carried out to determine the surface and oxidation states of the elements within the $w\mathbf{Zn_xCo_{1-x}Al}$ and $\mathbf{Zn_xCo_{1-x}Al}$ oxides (x = 0, 0.2, 0.4; see Fig. 5, 6, Fig. S21 and Table S1 of the ESI†), being corelated with the chemical composition of the spinel-type oxides determined from XRD data. The general and high-resolution XPS spectra were measured for both water-assisted and free oxides. As can be seen in Fig. 5, the general spectra revealed the occurrence of elemental peaks such as Zn 2p, Co 2p, Al 2s, O 1s and C 1s[67,68] whose concentration depends on the preparation method (water amount and x value).

For Co 2p high resolution data, the multiplet splitting and background subtraction, full width at half maximum (FWHM), relative shifts, relative intensities and component shape were considered.[69] Two multiplets were identified (Fig. 6), one corresponding to Co_3O_4 and the second one corresponding to Co^{2+} ions.[70] A significant concentration of Co_3O_4 oxide occurred on the surface of the water-added samples, $w\mathbf{Co_{1-x}Zn_xAl}$, and the Co 2p XPS spectra showed an increased amount of spinel-type cobalt(II/III) oxide (Fig. 6, left). Conversely, only a small amount of Co_3O_4 was identified on the surface of the materials, in the case of the water-free samples, $\mathbf{Zn_xCo_{1-x}Al}$ (Fig. 6, right).

The high-resolution O 1s spectra reveal the presence of four O-containing species in all samples (Fig. 7). The first two components observed at low binding energies ~530.6 eV and ~531.5 eV can be assigned to the O^{2-} from the Co/Zn–O bond and O^{2-} from the aluminum oxide bond, respectively.[71] The third (*ca.* 532.3 eV) and the fourth (*ca.* 533.3 eV) components are assigned to the hydroxyl group and H_2O adsorbed surface, respectively.[71] The zinc-enriched $\mathbf{Zn_xCo_{1-x}Al}$ (x = 0.2, 0.4) oxides have the highest number of Al–O bonds at the surface. The Al 2p XPS spectra (Fig. 8, left) are shifted up to 1 eV,

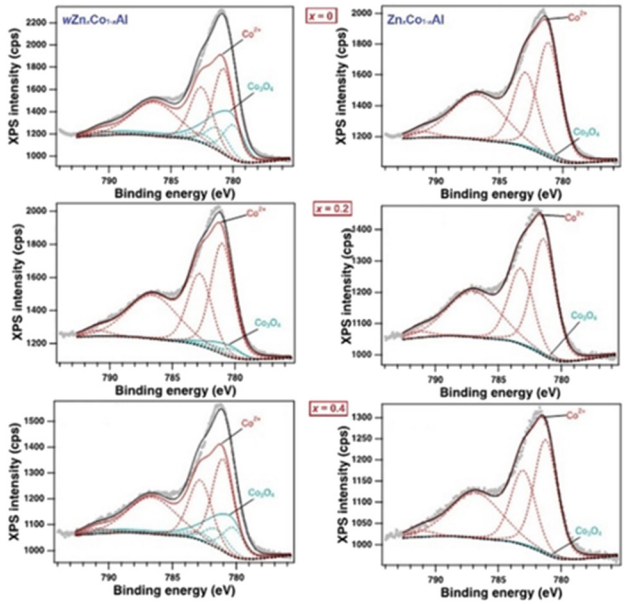

Fig. 7 High-resolution O 1s XPS of the water-assisted $w\mathbf{Zn_xCo_{1-x}Al}$ and water-free $\mathbf{Zn_xCo_{1-x}Al}$ oxides (x = 0, 0.2 and 0.4).

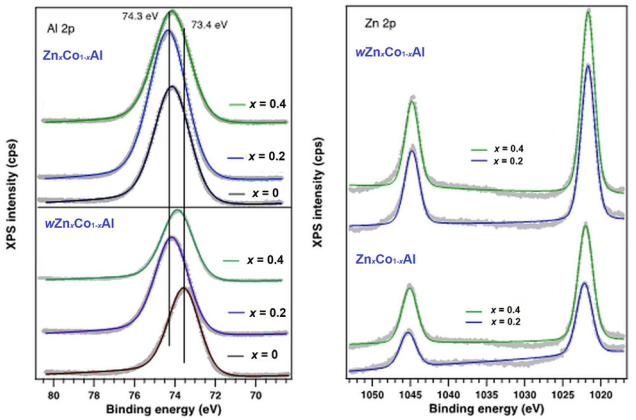

Fig. 8 High-resolution: Al 2p (left) and Zn 2p (right) XPS of the water-assisted $w\mathbf{Zn_xCo_{1-x}Al}$ and water-free $\mathbf{Zn_xCo_{1-x}Al}$ oxides (x = 0, 0.2 and 0.4).

depending on the type of aluminum-containing phase. Thus, Al^{3+} ions from the spinel aluminum oxide are usually identified at high values of binding energies (74.3 eV) and have a wider FWHM (~2.1 eV), while aluminum(III) ions from $CoAl_2O_4$ are found at lower values of binding energies (73.4 eV) and have a lower FWHM (with 0.2–0.3 eV).[72]

One can observe that stoichiometric $w\mathbf{Zn_xCo_{1-x}Al}$ (x = 0) has the largest amount of $CoAl_2O_4$ on the surface, while for the Zn-doped water-free oxide, $Zn_xCo_{1-x}Al$ (x = 0.2), the main material on the surface is aluminum oxide. For $w\mathbf{Zn_xCo_{1-x}Al}$ (x = 0.2, 0.4) and $\mathbf{Zn_xCo_{1-x}Al}$ (x = 0, 0.4) an intermediate ratio of the two aluminum-based phases is established. The Zn 2p high resolution spectra (Fig. 8, right) indicate the presence of Zn^{2+} found at ~1021.9 eV (Zn 2p3/2).[72,73] No significant changes are observed in the binding energies of both series of the oxides, confirming that the oxidation state is preserved.

The XPS results show that the surface composition of $w\mathbf{Zn_xCo_{1-x}Al}$, and water free $\mathbf{Zn_xCo_{1-x}Al}$ oxides (x = 0, 0.2 and 0.4) follows the same trend observed in XRD analysis (on the bulk sample): a predominance of Co-based spinels for water-assisted samples and, for $\mathbf{Zn_xCo_{1-x}Al}$ oxides, of aluminum oxide.

Morphological analysis

SEM analysis. The amount of water added to the reaction had a strong impact on the morphology of the calcination products. Thus, the SEM micrographs of the $w\mathbf{Zn_xCo_{1-x}Al}$ oxides revealed the formation of large, irregular micro-aggregates of nanoparticles whose dimensions vary from 5 up to 100 μm. For x = 0 (Fig. 9a–c), the sizes of the aggregates range between 5 and 50 μm and consist of small, spherical nanoparticles. The incorporation of zinc ions into the spinel lattice led to larger, more compact micro-aggregates (Fig. 9d, e, g and h) of nanoparticles (Fig. 9f and i). A rough estimation indicates that the particle size ranges between 8 and 30 nm.

The $\mathbf{Zn_xCo_{1-x}Al}$ oxides exhibit a completely different morphology compared to their water-assisted analogues. Therefore, the zinc-free powder exhibits smaller micro-sized aggregates (from 1 up to *ca.* 5 μm) with a narrower size distribution, showing silkworm hierarchical cocoon-like shapes composed of very small, spherical particles of $Co_3O_4/CoAl_2O_4$, covered with large flakes of $Al_{2.67}O_4$ (Fig. 10a–f). Generally, the cocoon-type morphology is quite rare for metal oxides[74–78] and, to our knowledge, this is the first report of spinel structures with such a hierarchical architecture. For the zinc-containing samples, the aluminum oxide amount shows a significant increase, and the flakes completely cover the zinc/cobalt aluminate cores (Fig. 10d–i). However, FE-SEM investigation is not powerful enough to reveal the structure of these flakes.

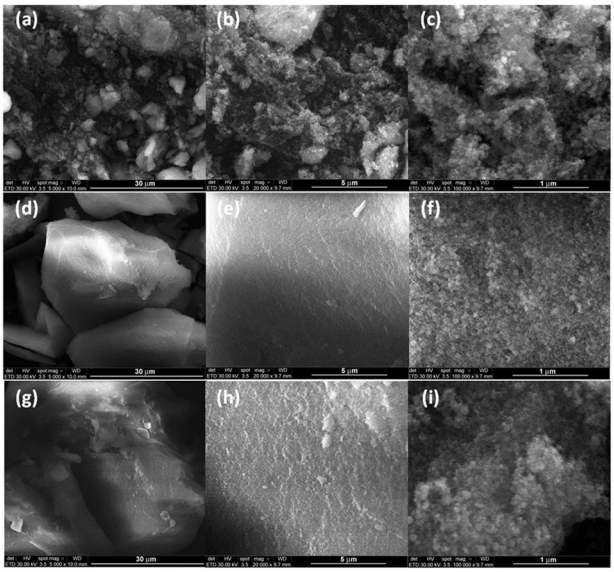

Fig. 9 SEM images at different magnifications of water-added $w\mathbf{Zn_xCo_{1-x}Al}$ oxides: (a–c) x = 0; (d–f) x = 0.2 and (g–i) x = 0.4.

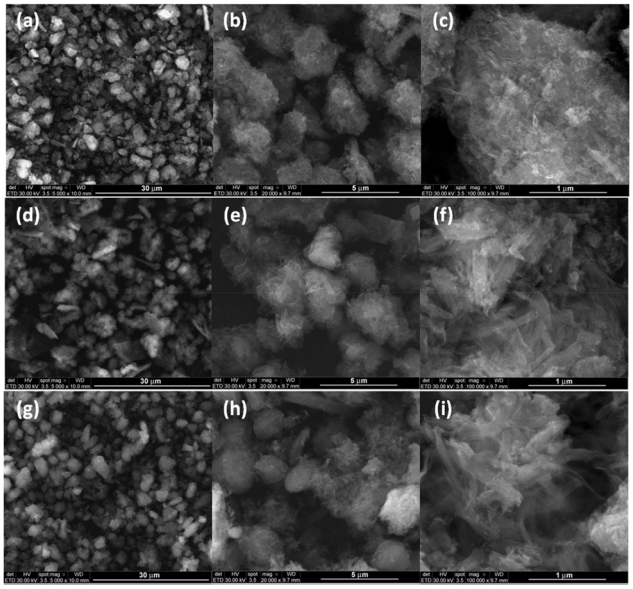

Fig. 10 SEM images at different magnifications of water-free $Zn_xCo_{1-x}Al$ oxides: (a–c) x = 0; (d–f) x = 0.2, and (g–i) x = 0.4.

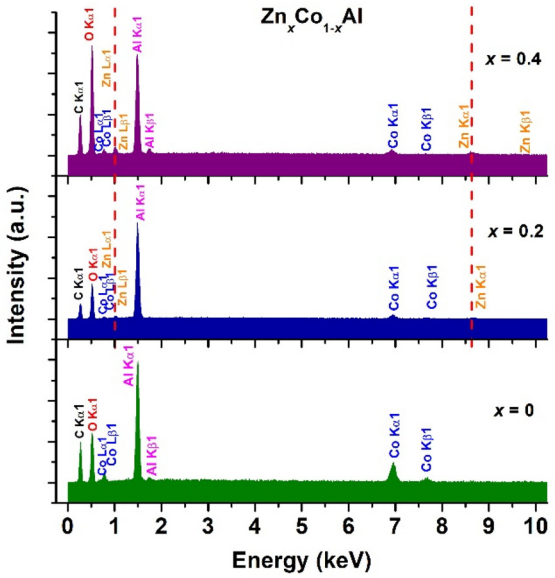

Fig. 12 EDX spectra of (top) water-free $Zn_xCo_{1-x}Al$ oxide powders (x = 0, 0.2, 0.4).

The EDX spectra of both $wZn_xCo_{1-x}Al$ and $Zn_xCo_{1-x}Al$ oxides confirm the incorporation of zinc ions for the powders with x = 0.2 and x = 0.4 (Fig. 11, 12 and Table S2 in the ESI†). The exclusive presence of the Co, Zn, Al and O species that make up the spinel phases rules out any contamination during the synthesis process.

TEM, HRTEM and SAED analyses. In order to have a more realistic image of the morphological details, such as: (i) the size and shape of particles of the different spinel phases obtained by both synthesis paths, (ii) interdistribution of these phases in the powders and (iii) the flake structure for the water-free $Zn_xCo_{1-x}Al$ oxides, TEM/HRTEM analyses coupled with EDX mapping in STEM mode are required.

The TEM image of the water-added $wZn_xCo_{1-x}Al$ powder reveals the presence of polyhedral spinel particles, with well-defined boundaries and sizes ranging between 7 and 43 nm (Fig. 13a). The Zn^{2+} addition seems to determine a slight particle size decrease, a higher homogeneity in the size of particles, as well as a gradual change of their shape toward a more rounded morphology as the zinc content increases

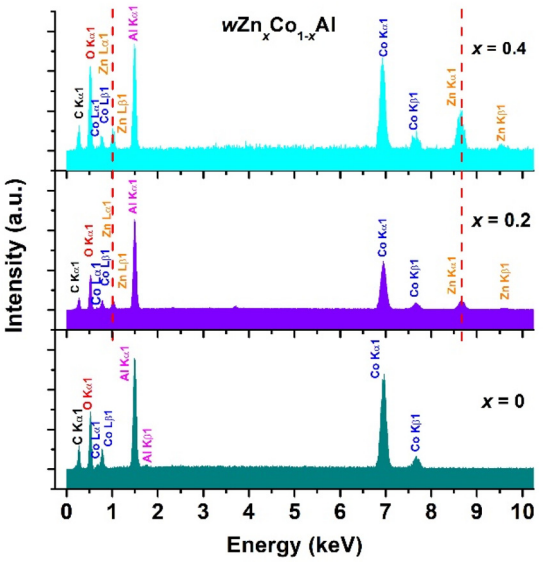

Fig. 11 EDX spectra of water-added $wZn_xCo_{1-x}Al$ oxide powders (x = 0, 0.2, 0.4).

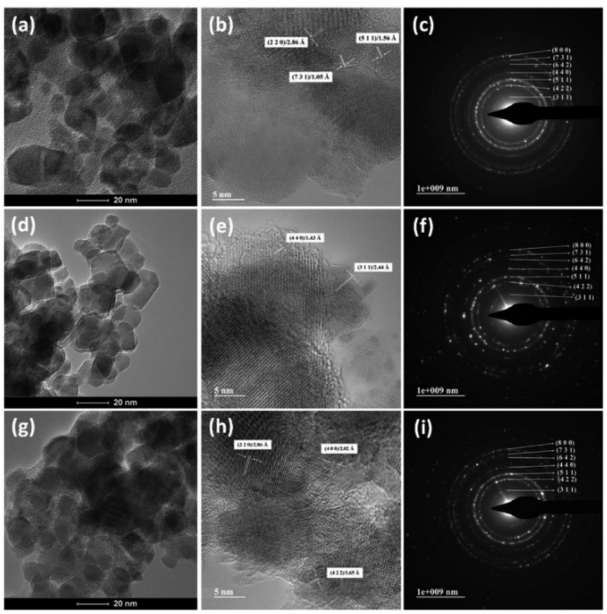

Fig. 13 (a), (d) and (g) TEM images; (b), (e) and (h) HRTEM images and (c), (f) and (i) SAED patterns of the water-added $wZn_{1-x}Co_xAl$ powders: (a)–(c) x = 0; (d)–(f) x = 0.2 and (g)–(i) x = 0.4.

(Fig. 13d and g). The HRTEM images (Fig. 13b, e and h) of the ***w*Zn$_x$Co$_{1-x}$Al** particles show long-range ordered fringes which prove their high crystallinity degree. The aspect of the concentric dashed diffraction rings, consisting of well-defined bright spots in the corresponding SAED patterns (Fig. 13c, f and i), confirms the observations from the HRTEM images regarding the crystallinity of these samples.

Significant changes in the morphology and crystallinity of the particles were noticed for the water-free **Zn$_x$Co$_{1-x}$Al** powders (Fig. 14a, d and g). Thus, for the zinc-free sample (x = 0), the TEM image of Fig. 11a shows a duplex-type morphology, due to the coexistence of small particles (7–13 nm) and larger ones (30–40 nm), belonging, most likely, to different spinel phases.

Indeed, for the sample with Zn^{2+} content corresponding to the substitution degree of x = 0.2 for which, according to the XRD results, the formation of cobalt-containing spinel phases ($CoAl_2O_4$ and Co_3O_4) is suppressed, so that almost only aluminum-based spinel was identified (see Table 1). The corresponding TEM image of Fig. 14d reveals the exclusive presence of small particles (≤13 nm), which allowed us to conclude that they belong to the $Al_{2.67}O_4$ phase. It is worth mentioning that these small $Al_{2.67}O_4$ particles are agglomerated comprising the thin and transparent flakes noticed in the related FE-SEM image (see Fig. 10f). For the sample with the highest Zn^{2+} content (x = 0.4), where the amount of $Al_{2.67}O_4$ spinel still prevails over the amounts of the secondary $CoAl_2O_4$ and Co_3O_4 phases, the powder morphology is somewhat similar to the one corresponding to the sample **Zn$_x$Co$_{1-x}$Al** (x = 0.2) already discussed above (Fig. 14g). Unlike the water-added samples, in this case, the significantly lower size of the particles strongly affects the crystallinity degree, especially for the Zn^{2+}-containing powders, as the HRTEM images of Fig. 14b, e and h as well as the more diffuse diffraction rings from the SAED patterns of Fig. 14c, f and i suggest.

The STEM images together with the overall and elemental EDX maps for the water-added ***w*Zn$_x$Co$_{1-x}$Al** (x = 0, Fig. 15 and x = 0.2, Fig. 16) samples show the presence of all the three spinel phases: $Zn_xCo_{1-x}Al_2O_4$ (**A**), Co_3O_4 (**B**) and $Al_{2.67}O_4$ (**C**), in agreement with the results concerning the phase composition obtained by the Rietveld analysis presented in Table 1.

EDX investigations were also performed on the water-free **Zn$_x$Co$_{1-x}$Al** (x = 0, Fig. 17 and x = 0.2, Fig. 18) powders. For the Zn^{2+}-free powder, it is obvious that the thin flakes denoted as **C** in Fig. 17 are exclusively built up of very small $Al_{2.67}O_4$ particles, while larger Co_3O_4 particles (**B**) seem to grow on the particles belonging to the major $CoAl_2O_4$ phase (**A**).

The EDX mapping of the region displayed in the STEM image of Fig. 18 reveals that the **Zn$_x$Co$_{1-x}$Al** (x = 0.2) powder

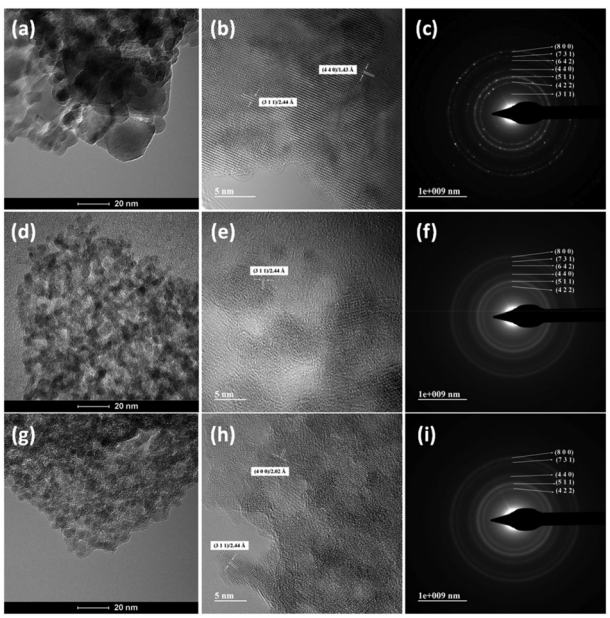

Fig. 14 (a), (d) and (g) TEM images; (b), (e) and (h) HRTEM images and (c), (f) and (i) SAED patterns of the water-free **Zn$_{1-x}$Co$_x$Al** powders: (a)–(c) x = 0; (d)–(f) x = 0.2 and (g)–(i) x = 0.4.

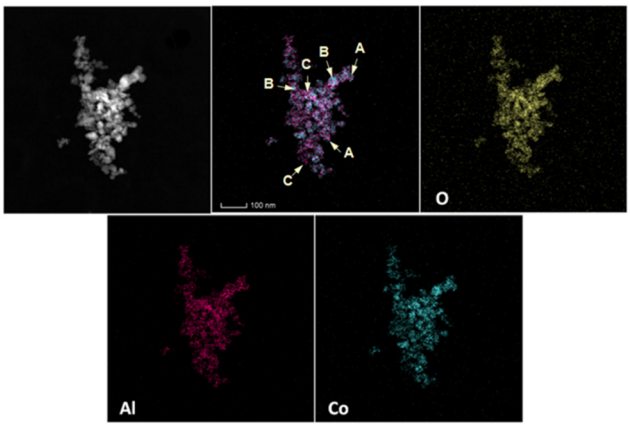

Fig. 15 STEM image and the overall and elemental EDX maps of the water-added ***w*Zn$_x$Co$_{1-x}$Al** powder (x = 0, **A** – $CoAl_2O_4$; **B** – Co_3O_4 and **C** – $Al_{2.67}O_4$).

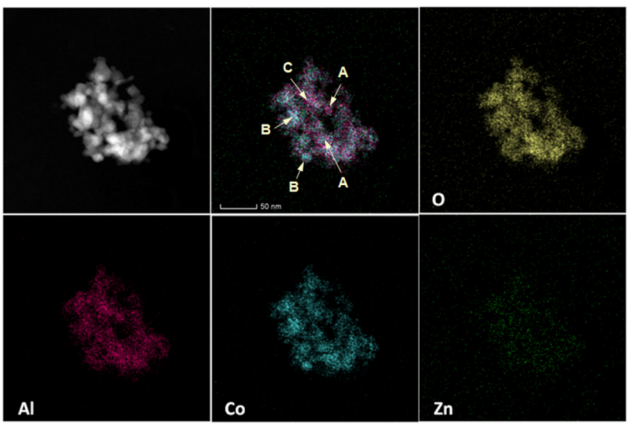

Fig. 16 STEM image and the overall and elemental EDX maps of the water-added ***w*Zn$_x$Co$_{1-x}$Al** powder (x = 0.2, **A** – $Zn_{1-x}Co_xAl_2O_4$; **B** – Co_3O_4 and **C** – $Al_{2.67}O_4$).

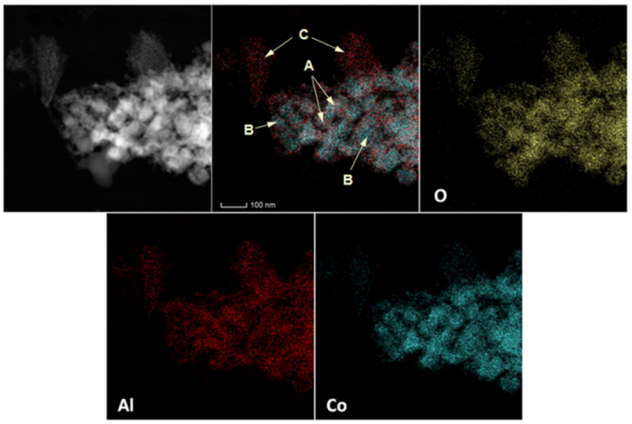

Fig. 17 STEM image and the overall and elemental EDX maps of the water-free $Zn_xCo_{1-x}Al$ powder (x = 0, **A** – $Zn_{1-x}Co_xAl_2O_4$; **B** – Co_3O_4 and **C** – $Al_{2.67}O_4$).

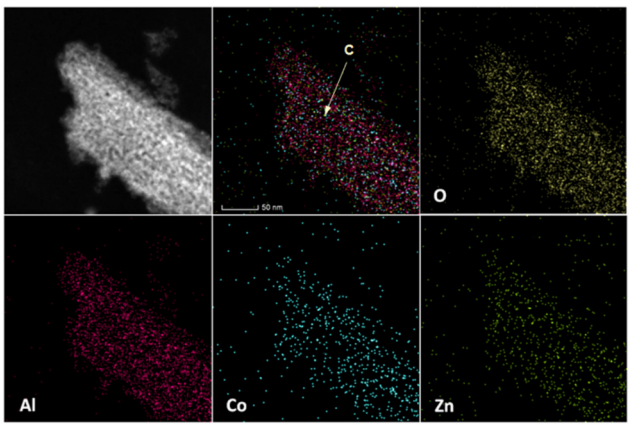

Fig. 18 STEM image and the overall and elemental EDX maps of the $Zn_xCo_{1-x}Al$ powder (x = 0.2, **A** – $Zn_xCo_{1-x}Al_2O_4$; **B** – Co_3O_4 and **C** – $Al_{2.67}O_4$).

consists almost entirely of rows of nanoparticles assembled in thin, planar $Al_{2.67}O_4$ flakes. All these results are also in good agreement with the XRD data and SEM/TEM observations presented above.

Proposed reaction mechanism. The composition of the two types of Zn/Co/Al-based oxides is clearly influenced by the differences between the two types of precursors resulting from the reflux reactions. Previous results showed that the hydrolysis process of different starting metal salts in polyols, including cobalt(II) acetate and aluminum(III) hydroxyacetate salts, yielded either metal alkoxide complexes[79] or layered hydroxide metal acetates.[80] Besides, different approaches, including molecular orbital calculations, developed to gain more insights into the formation of metal nanoparticles, highlighted the importance of the dissociation constants of the metal sources (salts or complexes) as well as the polyol peculiarities, like (branched) alkyl chain length and the number of hydroxyl group positions on the aliphatic chains.[44,81–89]

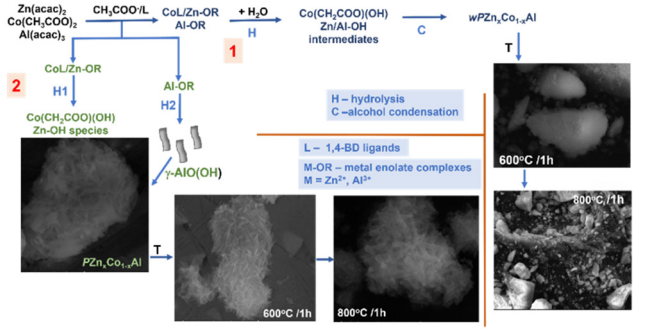

Scheme 1 Possible reaction pathways for the formation of water-assisted, ***w*PZn$_x$Co$_{1-x}$Al**, and water free precursors, ***P*Zn$_x$Co$_{1-x}$Al**, and of their corresponding calcination products, ***w*PZn$_x$Co$_{1-x}$Al** and **Zn$_x$Co$_{1-x}$Al**.

Scheme 1 shows the possible reaction pathways for the two series of oxides. The reaction conditions for obtaining the water-assisted ***w*PZn$_x$Co$_{1-x}$Al** and water-free ***P*Zn$_x$Co$_{1-x}$Al** precursors are similar (temperature/time of reaction and metal salt/complex concentrations), the water amount from the reaction being the only variable. The synthesis starts with the dissolution of the cobalt/zinc and aluminum salts/complexes, followed by the *in situ* formation of intermediates that further undergo hydrolysis reaction (**H**).

The chemical conversion of the cobalt/zinc and aluminum sources is strongly influenced by the different dissociation rates of the metal/salt complexes, and the reaction kinetics is expected to decrease in the following order: $Co(CH_3COO)_2$ > $Zn(acac)_2$ > $Al(acac)_3$. The cobalt acetate, with the highest dissociation constant,[85] will firstly release CH_3COO^- anions, whereas $Al(acac)_3$ will be the last to dissociate, being much less labile due to the strong Lewis acid character of Al^{3+} cations and the three chelating $(acac)^-$ ligands.[81–85] At the same time, 1,4-BD could act as a ligand toward the metal ions to form complexes. Most likely, the resulting polyol-derived and/or cobalt alkoxide complexes will subsequently evolve into layered cobalt hydroxyacetate species.[83] Conversely, the metal acetylacetonates (Zn/Al) undergo hydrolysis *via* metal enolate complexes that are further hydrolyzed to form M-OH chemical species, with the release of acetone.[79,80]

The hydrolysis ratio (h) represents the critical factor that causes the differences between the two series of precursors, ***w*PZn$_x$Co$_{1-x}$Al** and ***P*Zn$_x$Co$_{1-x}$Al**. In the case of water-assisted synthesis (h = 1.2), the hydrolysis process in 1,4-BD is driven by water in a similar way to the aqueous sol–gel processes,[86–88] affording dark-blue gels of ***w*PZn$_x$Co$_{1-x}$Al** (**pathway 1** in Scheme 1).

As indicated by the FTIR spectra, in the water-assisted precursors multiple chemical species co-exist: hydroxyacetate, alkoxide and hydroxide intermediates and, also, Zn/Co–O–Al based units resulting from the alcohol condensation reactions (**C**, see Scheme 1, **pathway 1**). The thermal treatment gave rise to aggregates of nanoparticles of three-component spinel oxides, $Zn_x/Co_{1-x}Al_2O_4$, Co_3O_4 and $Al_{2.67}O_4$. Interestingly, the

increase of the x value determines a predominance of zinc/cobalt-aluminate spinels (up to 83.3%, see Table 1). This trend in the composition of the material is likely to result from the strong preference of cobalt(II) and zinc(II) for the tetrahedral sites that favors the formation of the spinel aluminate. It is worth mentioning that Co_3O_4 oxides are rarely obtained through the polyol method.[86,90,91]

For the ***PZn$_x$Co$_{1-x}$Al*** precursors, the necessary water for the hydrolysis processes results from two sources: crystallization water molecules from hydrated metal salts/complexes (cobalt(II) acetate and zinc(II) acetylacetonate), as well as from the esterification reactions of 1,4-BD (**pathway 2** in Scheme 1). Nevertheless, the amount of water generated is insufficient to produce gels, as in water-added reactions, the final products being in the form of light-green powders precipitating from dark-blue solutions. Under such conditions, the nature of the starting materials becomes important, and the different dissociation constants of the reactants ($Al(acac)_3$, $Zn(acac)_2$ and $Co(CH_3COO)_2$) explain the simultaneous formation of two phases, Zn/Co-containing intermediates[52] and boehmite (see Fig. S2 of the ESI†). Thus, the formation of the ***PZn$_x$Co$_{1-x}$Al*** precursors is likely to follow a three-step process, taking into account the stability of the starting materials: (1) the formation of Co^{II}/Zn^{II} intermediate complexes, followed by the Co(II) hydroxyacetate and Zn–OH species (**H1**); (2) the subsequent formation of the Al(III) complexes that will be layered upon the Co(II)/Zn(II) intermediates and (3) the preferential hydrolysis of the outer Al(III) complexes (**H2**). However, the dark-blue colored solutions indicate that a part of the cobalt cations remains in solution, most likely as soluble, stable complexes of cobalt(II) ions and, therefore, the initial stoichiometries (molar ratios) of the zinc/cobalt/aluminum metals will not be the same as those corresponding to ***PZn$_x$Co$_{1-x}$Al*** precursors. The hydrolysis process of the aluminum(III) intermediates yields γ-AlO(OH),[89] the flakes of boehmite being attached to the already formed zinc/cobalt intermediates to give rise to silkworm-cocoon-like aggregates (Scheme 1). The thermolysis of the ***PZn$_x$Co$_{1-x}$Al*** precursors at 800 °C generates the defect spinel $Al_{2.67}O_4$ through dehydration of γ-AlO(OH), preserving the flake-like morphology, *via* a topotactic decomposition.[92] Due to the strong preference of the Al^{3+} for the octahedral environment, during the thermal processing, the Zn^{II}/Co^{II} cations could diffuse and easily occupy the tetrahedral sites within the $Al_{2.67}O_4$ spinel lattice to form simultaneously the isostructural zinc/cobalt aluminate phase,[93] affording heterostructures with a unique core–shell arrangement: cobalt aluminate aggregate cores within flake-like aluminum oxide shells. The zinc(II)-incorporation process is accompanied by an increase of $Al_{2.67}O_4$ quantity for x = 0.2, 0.4 which completely embeds the zinc/cobalt cores.

In conclusion, the two reaction pathways and, consequently, the nature of the precursors and the composition of their calcination products depend on the water amount in the reaction, the zinc-incorporation process and the stereochemical preference of the metal ions for the tetrahedral/octahedral sites of the spinel lattice:

- for the water-added synthesis, the Zn/Co–O–Al intermediate units (resulting from the alcohol polycondensation reaction) acted as centers of nucleation for Zn/Co-based spinels. The homogeneous distribution of the Zn/Co centers of nucleation in gels together with the strong preference of Zn(II)/Co(II) to occupy the tetrahedral sites of the spinel lattice favor, after the post-synthesis calcination treatment, the formation and predominance of the Co-based spinel crystalline phases.

- for the water free synthesis, the formation of ***PZn$_x$Co$_{1-x}$Al*** precursors (light green powders) is influenced by the dissociation constant of the starting materials. Thus, the slow hydrolysis of $Al(acac)_3$ with the formation of flake-like γ-AlOOH (boehmite) embedded the incipient Zn/Co–Al intermediates. Surprisingly, the addition of Zn and the corresponding diminishing of Co amount has a reversed effect compared to the water-assisted analogues and led to Zn/Co-cation deficient precursors ***PZn$_x$Co$_{1-x}$Al*** whose thermolysis process led to spinel mixtures in which the aluminum oxide prevailed.

Specific surface area and porosity analysis. Porosity and specific surface area investigations were carried out to probe the textural properties of the two types of spinels that could influence the chromatic performances of the samples. The water content and the incorporation of zinc(II) ions into the spinel lattice strongly influences the textural properties of the oxides (sizes of specific surfaces, the pore structure and their distribution; see Table 2 and Fig. S22–S27 in the ESI†).

The N_2 adsorption–desorption isotherms are of type IV according to IUPAC classification and indicate mesoporous materials.[94] Depending on the amount of water in the reaction mixture (water-added/water-free), the isotherms show two different types of hysteresis loops that could be further correlated with different pore structures. Thus, for ***w*Zn$_x$Co$_{1-x}$Al** oxides, the isotherms exhibit relatively wide and asymmetrical hysteresis loops of type H2 with an adsorption branch characteristic of a broad pore size distribution (PSD) and a steeper evaporation branch (Fig. S22–S24 in the ESI†). This type of hysteresis loop is specific for materials with complex pore networks,[94] and their asymmetry suggests an interaction mechanism between pores during the desorption process.[95] The zinc(II) incorporation determines an enlargement of PSD (~4–20 nm *vs.* 3 to 15 nm) and a shift toward higher values of the peak maxima (~9 nm *vs.* 14 nm). For **Zn$_x$Co$_{1-x}$Al** oxides, the hysteresis loops are of type H3, specific to slit-like pore

Table 2 Textural properties (total pore volume and specific surface area) of ***w*Zn$_x$Co$_{1-x}$Al** and **Zn$_x$Co$_{1-x}$Al** oxides (x = 0, 0.2, 0.4)

Sample	Total pore volume ($cm^3\ g^{-1}$)	Specific surface area, S_{BET} ($m^2\ g^{-1}$)
***w*Zn$_x$Co$_{1-x}$Al**		
x = 0	0.37	141.7
x = 0.2	0.21	60.3
x = 0.4	0.13	39.8
Zn$_x$Co$_{1-x}$Al		
x = 0	0.37	167.3
x = 0.2	0.46	199.2
x = 0.4	0.57	208.4

shapes, in aggregates of plate-like particles that lose their assemblage (Fig. S25–S27 in the ESI†).[94] In this case, the incorporation of zinc ions into the spinel lattice seems to induce less disorder and inhomogeneity of the pore system. Thus, for $x = 0$, the PSD is wide, ranging from 4 to 30 nm, while for zinc-containing oxides it is narrower, ranging from 3 to 12 nm for $x = 0.2$ and from 3 to 20 nm for $x = 0.4$. The textural properties of the two types of cobalt aluminate samples correspond well to the morphological analysis results.

The **$Zn_xCo_{1-x}Al$** mixed oxides exhibit considerably larger areas compared with water-assisted analogues, the surface increasing with the zinc(II) concentration due to the increased concentration of the defect spinel $Al_{2.67}O_4$. Examples of cobalt aluminate-based oxides with high specific areas are very rare and were obtained *via* different soft chemistry synthesis (sol–gel,[96,97] thermal decomposition of Co–Al hydrotalcite,[98] and evaporation induced self-assemble methods[99]) or supporting the mixed oxides on γ-Al_2O_3.[100] The water-added analogues, ***w*Zn$_x$Co$_{1-x}$Al**, exhibit higher S_{BET} values than most of the reported examples of metal aluminates. Besides, the gradual zinc-incorporation causes a reversed evolution compared to the case of water-free derivatives, with the S_{BET} values decreasing with the incorporation degree, probably due to a more compact assembly of oxide nanoparticles and increased crystallite sizes.

Spectral analysis. The FTIR spectra of the two series of oxides, ***w*Zn$_x$Co$_{1-x}$Al** and **Zn$_x$Co$_{1-x}$Al**, show typical absorptions of Co–O, Al–O and Co–O–Al vibration modes in the spinel lattice (660–490 cm^{-1}),[101] as well as water and carbonaceous residue (see discussions and Fig. S28–S30 of the ESI†). NIR-UV-Vis spectra of the water-added and water-free oxides (Fig. S31 and S32 and discussion in the ESI†) exhibit bands attributed to band-to-band electron excitations (in the UV domain), O(p) → Al(s)/Zn(p) excitations, and visible and NIR absorptions from $[Co^{II}O_4]_{Td}/[Co^{II}O_6]_{Oh}$ and $[Co^{III}O_6]_{Oh}$ chromophores.[74–78,100,102,103] The broader visible absorption for ***w*Zn$_x$Co$_{1-x}$Al** oxides is likely due to the high concentration of spinel Co_3O_4 from these samples.

Coloring properties. The color purity of the ***w*Zn$_x$Co$_{1-x}$Al** and **Zn$_x$Co$_{1-x}$Al** oxides was evaluated by analyzing the color ($L^*a^*b^*$) and chroma (C^*) parameters (Table 3, Fig. 19 and Fig. S33 in the ESI†). The L^*, a^* and b^* values give the pigment lightness (L^*) and the degree of red (a^*) and yellow (b^*) colors, whereas the chroma (C^*) parameter represents the degree of color purity and saturation. For all samples, the values of the lightness parameter (L^*) are small, showing a low degree of luminosity of the pigments, with more intense colors (the higher the L^* value, the lighter the sample; the lower the L^* value, the brighter or more intense the color). The water-free oxides are lighter than the water-added analogues. The zinc-enriched **Zn$_x$Co$_{1-x}$Al** oxides ($x = 0.2$, 0.4) have the highest L^* values and blue color yields defined by the minimum value of the b^* parameter. These results prove that the chromatic performances of the pigments are clearly improved for zinc–cobalt aluminates, the b^* values being remarkably high compared to the measurements reported previously.[34,104,105] The best coloring characteristics correspond to the **Zn$_x$Co$_{1-x}$Al** ($x = 0.2$) pigment composition.

Table 3 Colorimetric coordinates of ***w*Zn$_x$Co$_{1-x}$Al** and **Zn$_x$Co$_{1-x}$Al** ($x = 0$, 0.2, 0.4)

Sample	L^*	a^*	b^*	C^*
***w*Zn$_x$Co$_{1-x}$Al**				
$x = 0$	6	3	−28	28.16
$x = 0.2$	6	3	−27	27.16
$x = 0.4$	6	3	−27	27.16
Zn$_x$Co$_{1-x}$Al				
$x = 0$	12	−10	−43	44.14
$x = 0.2$	14	11	−94	94.64
$x = 0.4$	14	7	−88	88.27

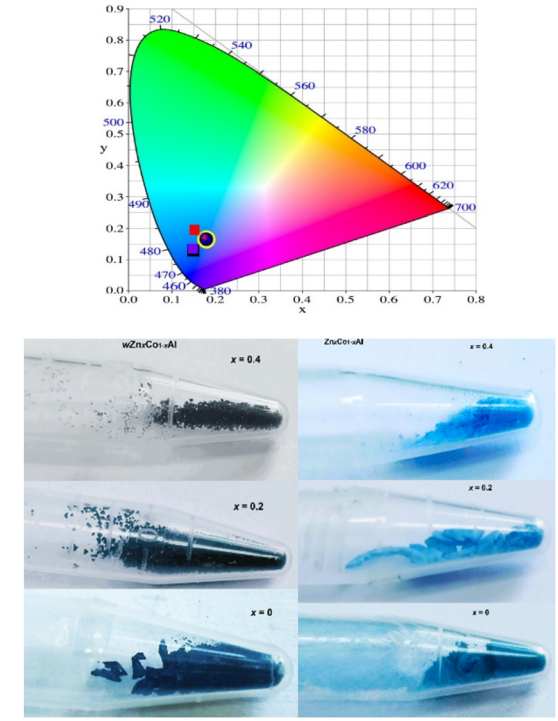

Fig. 19 (Top) Color coordinates of ***w*Zn$_x$Co$_{1-x}$Al** ($x = 0$, 0.2, 0.4; yellow/pink/navy-filled dots) and **Zn$_x$Co$_{1-x}$Al** oxides ($x = 0$ – red-filled, 0.2 – black-filled, and 0.4 – magenta-filled squares); (bottom) pictures of water-assisted ***w*Zn$_x$Co$_{1-x}$Al** and water-free **Zn$_x$Co$_{1-x}$Al** as-obtained oxides.

The water-assisted oxides have closed values of the colorimetric parameters, with no significant influence of the zinc incorporation within the spinel lattice. All chromatic coordinates of ***w*Zn$_x$Co$_{1-x}$Al** oxides are lower compared to those of **Zn$_x$Co$_{1-x}$Al** samples, meaning that the water-assisted samples are lighter and less blue and have a lower degree of color saturation than the water-free oxides. Nevertheless, considering the large negative values of b^* parameters, the samples are blue shifted.

Conclusions

Two new series of mesoporous spinel-type oxides were obtained through a two-step approach: the hydrolysis of

Zn_x^{II}/Co_{1-x}^{II} and Al^{III}-based salts/complexes in 1,4-butanediol followed by a calcination treatment (x = 0, 0.2, 0.4). For all oxide samples, the XRD analysis Raman and XPS spectroscopy revealed the co-existence of three isostructural spinel crystalline phases: $Zn_xCo_{1-x}Al_2O_4$, Co_3O_4 and $Al_{2.67}O_4$. The composition and morpho-structural features of the spinel oxides strongly depend on the water amount added for the polyol-assisted synthesis, as well as on the zinc-doping process. Thus, a reaction in which a small amount of water was added led to gels and further, after the thermal treatment, to irregular aggregates of oxide nanoparticles. For the zinc-enriched samples, $Zn_x/Co_{1-x}Al_2O_4$ phases predominate. Conversely, in a similar water-free synthesis, light green powders were obtained, whose thermolysis gave rise to intense blue spinel oxide nanoparticles, with very small sizes and with a unique silkworm cocoon morphology. For x = 0.2 and 0.4 a significant increase of the aluminum oxide phase content occurred. Our results opened new and interesting perspectives in designing "green" inorganic pigments with a beneficial impact on health, environment, and economy which are outlined here: (i) new compositions for spinel-type pigments; (ii) best coloring properties for a composition with the lowest content of cobalt; (iii) water amount representing the main element of control in polyol-assisted synthesis of spinels; and (iv) high S_{BET} values for water-free oxides due to the prevalence of the alumina phase which could help extend the area of applications toward other domains, like catalysis. But no conclusion can be more beautiful, motivating, and suitable as Vincent van Gogh words: "Cobalt is a divine color and there is nothing so beautiful to represent the atmosphere" (in a letter to his brother Theo).

Author contributions

M.-G. A.: investigation and writing – review & editing; A.-C. I.: methodology, writing – review & editing, and supervision; D. C. C., S. P., C. D. E., B. S. V., V. A. S., A.-I. N., F. N. and I. P.: investigation, formal analysis, and validation; D. V. and O. C.: methodology, conceptualization, writing – original draft/review & editing, resources, funding acquisition, project administration, and supervision.

Conflicts of interest

There are no conflicts to declare.

Acknowledgements

This work was supported by a grant of the Romanian Ministry of Education and Research, CNCS – UEFISCDI, project number PN-III-P4-ID-PCE-2020-2324, within PNCDI III. This work was carried out within the research program "Green chemistry for the synthesis of materials" of "Ilie Murgulescu" Institute of Physical Chemistry, Romanian Academy.

References

1 L. Gavilà, A. Lähde, J. Jokiniemi, M. Constanti, F. Medina, E. del Río, D. Tichit and M. G. Álvarez, *ChemCatChem*, 2019, **11**, 4944.
2 Y. Liu, L. Jia, B. Hou, D. Sun and D. Li, *Appl. Catal., A*, 2017, **530**, 30.
3 A. J. Reynoso, J. L. Ayastuy, U. Iriarte-Velasco and M. A. Gutiérrez-Ortiza, *Appl. Catal., B*, 2018, **239**, 86.
4 M. Mosleh, *J. Mater. Sci.: Mater. Electron.*, 2017, **28**, 773.
5 D. Visinescu, F. Papa, A. C. Ianculescu, I. Balint and O. Carp, *J. Nanopart. Res.*, 2013, **15**, 1456.
6 D. Li, Y. Li, X. Liu, Y. Guo, C.-W. Pao, J.-L. Chen, Y. Hu and Y. Wang, *ACS Catal.*, 2019, **9**, 9671.
7 L. Li, D. L. King, Z. Nie, X. S. Li and C. Howard, *Energy Fuels*, 2010, **24**, 3698.
8 Y. ElJabbar, H. Lakhlifi, R. ElOuatib, L. Er-Rakho, S. Guillemet-Fritsch and B. Durand, *J. Non-Cryst. Solids*, 2020, **542**, 120115.
9 S. D. Kapse, F. C. Raghuwanshi, V. D. Kapse and D. R. Patil, *Curr. Appl. Phys.*, 2012, **12**, 307.
10 J. P. Morán-Lázaroa, O. Blanco, V. M. Rodríguez-Betancourtt, J. Reyes-Gómez and C. R. Michel, *Sens. Actuators, B*, 2016, **226**, 518.
11 P. Panda, R. Mishra, S. Panigrahy and S. Barman, *ACS Appl. Nano Mater.*, 2022, **5**, 5176.
12 N. Srisawad, W. Chaitree, O. Mekasuwandumrong, P. Praserthdam and J. Panpranot, *J. Nanomater.*, 2012, 108369.
13 D. F. L. Horsth, J. O. Primo, N. Balaba, F. J. Anaissi and C. Bittencourt, *RSC Sustainability*, 2023, **1**, 159.
14 J. R. Hackman, in *Pigment Handbook, Volume 1: Properties and Economics*, ed. P. A. Lewis, Wiley-Interscience Publication, 2nd edn, 1988, p. 389.
15 A. Zhang, B. Mu, Z. Luo and A. Wang, *Dyes Pigm.*, 2017, **139**, 473.
16 Sh. Salem, *J. Ind. Eng. Chem.*, 2014, **20**, 818.
17 F. Tielens, M. Calatayud, R. Franco, J. M. Recio, J. Pérez-Ramírez and C. Minot, *J. Phys. Chem. B*, 2006, **110**, 988.
18 M. Taguchi, T. Nakane, K. Hashi, S. Ohki, T. Shimizu, Y. Sakka, A. Matsushita, H. Abe, T. Funazukuria and T. Naka, *Dalton Trans.*, 2013, **42**, 7167.
19 Z. Chen, E. Shi, W. Li, Y. Zheng and W. Zhong, *Mater. Lett.*, 2002, **55**, 281.
20 W. Li, J. Li and J. Guo, *J. Eur. Ceram. Soc.*, 2003, **23**, 2289.
21 T. Suzuki, H. Nagai, M. Nohara and H. Takagi, *J. Phys.: Condens. Matter*, 2007, **19**, 145265.
22 A. Maljuk, V. Tsurkan, O. Zeharko, A. Cervellino, A. Loidl and D. N. Argyriou, *J. Cryst. Growth*, 2009, **311**, 3997.
23 A. Stan, C. Munteanu, A. M. Musuc, R. Birjega, R. Ene, A. Ianculescu, I. Raut, L. Jecu, M. Badea-Doni, E. M. Angel and O. Carp, *Dalton Trans.*, 2015, **44**, 7844.
24 B. Serment, C. Brochon, G. Hadziioannou, S. Buffière, A. Demourguesa and M. Gaudon, *RSC Adv.*, 2019, **9**, 34125.
25 K. Mokhtari and Sh. Salem, *RSC Adv.*, 2017, **7**, 29899.

26 C. M. Alvarez-Docio, J. J. Reinosa, A. del Campo and J. F. Fernández, *Dyes Pigm.*, 2017, **137**, 1.
27 N. El Habra, L. Crociani, C. Sada, P. Zanella, M. Casarin, G. Rossetto, G. Carta and G. Paolucci, *Chem. Mater.*, 2007, **19**, 3381.
28 C. Feldmann and H. O. Jungk, *Angew. Chem., Int. Ed.*, 2001, **40**, 359.
29 A. Forés, M. Llusar, J. A. Badenes, J. Calbo, M. A. Tena and G. Monrós, *Green Chem.*, 2000, **2**, 93.
30 M. De Boeck, M. Kirsch-Volders and D. Lison, *Mutat. Res.-Fund. Mol. M.*, 2003, **533**, 135.
31 A. Yurdakul and H. Gocmez, *Ceram. Int.*, 2019, **45**, 5398.
32 J. Lu, K. Minami, S. Takami and T. Adschiri, *Chem. Eng. Sci.*, 2013, **85**, 50.
33 R. Dumitru, F. Manea, L. Lupa, C. Pacurariu, A. Ianculescu, A. Baciu and S. Negrea, *J. Therm. Anal. Calorim.*, 2017, **128**, 1305.
34 A. A. Ali, E. El Fadaly and I. S. Ahmed, *Dyes Pigm.*, 2018, **158**, 451.
35 A. Tirsoaga, D. Visinescu, B. Jurca, A. Ianculescu and O. Carp, *J. Nanopart. Res.*, 2011, **13**, 6397.
36 D. Visinescu, B. Jurca, A. Ianculescu and O. Carp, *Polyhedron*, 2011, **30**, 2824.
37 S. Zhao, J. Guob, W. Lia, H. Guo and B. You, *Dyes Pigm.*, 2018, **151**, 130.
38 D. Visinescu, C. Paraschiv, A. Ianculescu, B. Jurca, B. Vasile and O. Carp, *Dyes Pigm.*, 2010, **87**, 125.
39 D. Visinescu, G. Patrinoiu, A. Tirsoaga and O. Carp, in *Environmental chemistry for a sustainable world*, ed. E. Lichtfouse, J. Schwarbauer and D. Roberts, Springer, Dordrecht, Heidelberg, London, New York, 2013, ch. 5, p. 119.
40 T. C. de Sousa Santos, D. do Rosario Pinheiro, C. M. L. Costa, D. C. Estumano and N. F. da Paixão Ribeiro, *Ceram. Int.*, 2020, **46**, 2332.
41 R. Ianos, E. Muntean, C. Păcurariu, R. Lazău, C. Bandas and G. Delinescu, *Dyes Pigm.*, 2017, **142**, 24.
42 T. Nakane, T. Naka, K. Sato, M. Taguchi, M. Nakayama, T. Mitsui, A. Matsushita and T. Chikyowa, *Dalton Trans.*, 2015, **44**, 997.
43 N. Zhou, Y. Li, Y. Zhang, Y. Shu, S. Nian, W. Cao and Z. Wu, *Dyes Pigm.*, 2018, **148**, 25.
44 F. Fiévet, S. Ammar-Merah, R. Brayner, F. Chau, M. Giraud, F. Mammeri, J. Peron, J.-Y. Piquemal, L. Sicard and G. Viau, *Chem. Soc. Rev.*, 2018, **47**, 5187.
45 H. Dong, Y.-C. Chen and C. Feldmann, *Green Chem.*, 2015, **17**, 4107.
46 N. Pinna and M. Niederberger, *Angew. Chem., Int. Ed.*, 2008, **47**, 5292.
47 A. Kumar, A. Daverey, N. K. Sahu and D. Bahadur, *J. Mater. Chem. B*, 2013, **1**, 3652.
48 K. Vamvakidis, M. Katsikini, G. Vourlias, M. Angelakeris, E. C. Paloura and C. Dendrinou-Samara, *Dalton Trans.*, 2015, **44**, 5396.
49 J. Bai, X. Li, G. Liu, Y. Qian and S. Xiong, *Adv. Funct. Mater.*, 2014, **24**, 3012.
50 J. Merikhi, H.-O. Jungk and C. Feldmann, *J. Mater. Chem.*, 2000, **10**, 1311.
51 C. Feldmann, *Adv. Mater.*, 2001, **13**, 1301.
52 D. Visinescu, M. Scurtu, R. Negrea, R. Birjega, D. C. Culita, M. C. Chifiriuc, C. Draghici, J. Calderon Moreno, A. M. Musuc, I. Balint and O. Carp, *RSC Adv.*, 2015, **5**, 99976.
53 D. Visinescu, M. D. Hussien, J. Calderon Moreno, R. Negrea, R. Birjega, S. Somacescu, C. D. Ene, M. C. Chifiriuc, M. Popa, M. S. Stan and O. Carp, *Langmuir*, 2018, **34**, 13638.
54 A. A. Khassin, V. F. Anufrienko, V. N. Ikorskii, L. M. Plyasova, G. N. Kustova, T. V. Larina, I. Yu. Molina and V. N. Parmon, *Phys. Chem. Chem. Phys.*, 2002, **4**, 4236.
55 J. Zhang, S. Wei, J. Lin, J. Luo, S. Liu, H. Song, E. Elawad, X. Ding, J. Gao, S. Qi and C. Tang, *J. Phys. Chem. B*, 2006, **110**, 21680.
56 X. Bai, G. Caputo, Z. Hao, V. T. Freitas, J. Zhang, R. L. Longo, O. L. Malta, R. A. S. Ferreira and N. Pinna, *Nat. Commun.*, 2014, **5**, 5702.
57 U. Lavrenčič Štangar, B. Orel and M. Krajnc, *J. Sol-Gel Sci. Technol.*, 2003, **26**, 771.
58 M. Zayat and D. Levy, *Chem. Mater.*, 2000, **12**, 2763.
59 F. Tielens, M. Calatayud, R. Franco, J. M. Recio, J. Pérez Ramírez and C. Minot, *J. Phys. Chem. B*, 2006, **110**, 988.
60 A. M. Wahba, N. G. Imam and M. B. Mohamed, *J. Mol. Struct.*, 2016, **1105**, 61.
61 V. G. Hadjiev, M. N. Iliev and I. V. Vergilov, *J. Phys. C: Solid State Phys.*, 1988, L199.
62 C. M. Álvarez-Docio, J. J. Reinosa, A. Del Campo and J. F. Fernández, *J. Alloys Compd.*, 2019, **779**, 244.
63 B. Jongsomjit, J. Panpranot and J. J. Goodwin, *J. Catal.*, 2001, **204**, 98.
64 M. Bouchard and A. Gambardella, *J. Raman Spectrosc.*, 2010, **41**, 1477.
65 A. Rahman, M. S. Charoo and R. Jayaganthan, *Mater. Technol.*, 2015, **30**, 168.
66 J. Gangwar, B. K. Gupta, S. K. Tripathi and A. K. Srivastava, *Nanoscale*, 2015, **7**, 13313.
67 S. Petrescu, S. Avramescu, A. M. Musuc, F. Neatu, M. Florea and P. Ionita, *Mater. Res. Bull.*, 2020, **122**, 110643.
68 E. Pargoletti, U. H. Hossain, I. Di Bernardo, H. Chen, T. Tran-Phu, G. L. Chiarello, J. Lipton-Duffin, V. Pifferi, A. Tricoli and G. Cappelletti, *ACS Appl. Mater. Interfaces*, 2020, **12**, 39549.
69 M. C. Biesinger, B. P. Payne, A. P. Grosvenor, L. W. M. Lau, A. R. Gerson and R. St. C. Smart, *Appl. Surf. Sci.*, 2011, **257**, 2717.
70 A. Celebioglu, S. Vempati, C. Ozgit-Akgun, N. Biyikli and T. Uyar, *RSC Adv.*, 2014, **4**, 61698.
71 H. Jian-kang, J. Li-tao, H. Bo, L. De-bao, L. Yan and L. Ya-chun, *J. Fuel Chem. Technol.*, 2015, **43**, 846.
72 B. R. Strohmeier, *Surf. Sci. Spectra*, 1994, **3**, 128.
73 E. Agostinelli, C. Batistooni, D. Fiorani, G. Mattogno and M. Nogue, *J. Phys. Chem. Solids*, 1989, **50**, 269.

74 J. Ji, W. Zhu, J. Li, P. Wang, Y. Liang, W. Zhang, X. Yin, B. Wu and G. Li, *ACS Appl. Mater. Interfaces*, 2017, **9**, 19124.
75 F.-H. Du, Y. Ni, Y. Wang, D. Wang, Q. Ge, S. Chen and H. Y. Yang, *ACS Nano*, 2017, **11**, 8628.
76 J. Zhu, K. Y. Simon Ng and D. Deng, *ACS Appl. Mater. Interfaces*, 2014, **6**, 2996.
77 Q. Feng, M. Hirasawa, K. Kajiyoshi and K. Yanagisawa, *J. Mater. Sci.*, 2007, **42**, 640.
78 X. Yu, J. He, D. Wang, Y. Hu, H. Tian and Z. He, *J. Phys. Chem. C*, 2012, **116**, 851.
79 D. Larcher, G. Sudant, R. Patrice and J. M. Tarascon, *Chem. Mater.*, 2003, **15**, 3543.
80 L. Poul, N. Jouini and F. Fiévet, *Chem. Mater.*, 2000, **12**, 3123.
81 R. J. Joseyphus, T. Matsumoto, H. Takahashi, D. Kodama, K. Tohji and B. Jeyadevan, *J. Solid State Chem.*, 2007, **180**, 3008.
82 K. J. Carroll, J. U. Reveles, M. D. Shultz, S. N. Khanna and E. E. Carpenter, *J. Phys. Chem. C*, 2011, **115**, 2656.
83 T. Matsumoto, K. Takahashi, K. Kitagishi, K. Shinoda, J. L. Cuya Huaman, J.-Y. Piquemal and B. Jeyadevan, *New J. Chem.*, 2015, **39**, 5008.
84 K. Takahashi, S. Yokoyama, T. Matsumoto, J. L. Cuya Huaman, H. Kaneko, J.-Y. Piquemal, H. Miyamura and J. Balachandran, *New J. Chem.*, 2016, **40**, 8632.
85 H. Kaneko, T. Matsumoto, J. L. Cuya Huaman, M. Ishijima, K. Suzuki, H. Miyamura and J. Balachandran, *Inorg. Chem.*, 2021, **60**, 3025.
86 R. Deshmukh and M. Niederberger, *Chem. – Eur. J.*, 2017, **23**, 8542.
87 B. Ludi and M. Niederberger, *Dalton Trans.*, 2013, **42**, 12554.
88 J. Livage and C. Sanchez, *J. Non-Cryst. Solids*, 1992, **145**, 11.
89 S. Zhou, M. Antonietti and M. Niederberger, *Small*, 2007, **3**, 763.
90 L. T. Anh, A. K. Rai, T. V. Thi, J. Gim, S. Kim, V. Mathew and J. Kim, *J. Mater. Chem. A*, 2014, **2**, 6966.
91 A.-M. Cao, J.-S. Hu, H.-P. Liang, W.-G. Song, L.-J. Wan, X.-L. He, X.-G. Gao and S.-H. Xia, *J. Phys. Chem. B*, 2006, **110**, 15858.
92 W. Q. Jiao, X. M. Liang, Y. M. Wang and M. Y. He, *CrystEngComm*, 2014, **16**, 3348.
93 A. Dandapat and G. De Besides, *ACS Appl. Mater. Interfaces*, 2012, **4**, 228.
94 K. S. W. Sing, D. H. Everett, R. A. W. Haul, L. Moscou, R. A. Pierotti, J. Rouquerol and T. Siemieniewska, *Pure Appl. Chem.*, 1985, **57**, 603.
95 A. Grossman and C. Ortega, *Langmuir*, 2008, **24**, 3977.
96 E. Escalona Platero, C. Otero Areán and J. B. Parra, *Res. Chem. Intermed.*, 1999, **25**, 187.
97 C. Otero Areán, M. Peñarroya Mentruit, E. Escalona Platero, F. X. Llabrés i Xamena and J. B. Parra, *Mater. Lett.*, 1999, **39**, 22.
98 W. Xu, X. Liu, J. Ren, H. Liu, Y. Ma, Y. Wang and G. Lu, *Microporous Mesoporous Mater.*, 2011, **142**, 251.
99 L. Xu, J. Zhang, F. Wang, K. Yuan, L. Wang, K. Wu, G. Xua and W. Chen, *RSC Adv.*, 2015, **5**, 48256.
100 A. A. S. Gonçalves, M. J. F. Costa, L. Zhang, F. Ciesielczyk and M. Joroniec, *Chem. Mater.*, 2018, **30**, 436.
101 J. M. Saniger, *Mater. Lett.*, 1995, **22**, 109.
102 G. B. Kunde, G. D. Yadava and A. K. Ganguli, *J. Environ. Chem. Eng.*, 2019, **7**, 102834.
103 U. L. Stangar, B. Orel, M. Krajnc, R. C. Korošec and P. Bukovec, *Mater. Tehnol.*, 2002, **36**, 387.
104 A. Nakatsuka, Y. Ikeda, Y. Yamasaki, N. Nakayama and T. Mizota, *Solid State Commun.*, 2003, **128**, 85.
105 T. Tatarchuka, A. Shyichuk, J. Lamkiewicz and J. Kowalik, *Ceram. Int.*, 2020, **46**, 14674.